18   Modelling HVAC and renewable energy plant and control

Chris Underwood and Simon Rees

Scope

The chapter firstly presents an introduction to modern approaches to both steady-state and dynamic modelling of HVAC and related plant components and systems. Approaches to representations of components such as water-air heat exchangers are dealt with along with their representation in systems that include control elements are described. Common approaches to solving the resulting equations are also presented. A series of simulation case-studies are provided to illustrate the application of the methods. The chapter also presents examples of approaches to modelling the key components of a number of renewable energy systems that can be found integrated in buildings.

Learning outcomes

To be able to describe approaches to the modelling of HVAC, plant and renewable energy systems and their key components and how they can be represented mathematically and possible solution approaches. To be able to describe the data requirements of such modelling approaches and to execute calculations to find the state of example component models.

Key words

HVAC/ plant/ control/ renewable energy/ photovoltaic/ geothermal/ solar thermal/ wind power

---

Introduction

In this chapter, 'plant' is considered to be equipment included in a bßπuilding or a group of buildings for the purpose of generating and distributing energy with the ultimate aim of maintaining comfort as well as for the supply of essential services such as power, water supply and so on. A distinction is usually drawn to distinguish between energy generating plant or 'primary plant' and energy distributing plant or 'secondary plant'. Examples of the former include boilers, chillers, combined heat and power (CHP) modules, heat pumps, primary air handling units, solar collector arrays and photovoltaic arrays. Examples of secondary plant include room equipment such as radiator-convectors (or baseboard heaters), fan coil units and secondary air handling units, chilled ceilings, chilled beams and, conceivably, luminaires. Control systems designed to match the capacity to demand of these systems are, of course, to be found at both primary and secondary levels. The distinction can be important because, whereas secondary plant both influences and is influenced by the building rooms and zones within which the plant is located, primary plant merely responds to the demand places on it by the secondary systems. The primary plant does not directly interact with the building which means that it can often be modelled in isolation provided the load demands to be met are known. Developments in equation-based methods (in which the fundamental objects are mathematical equations) can therefore play a role in certain types of plant modelling to get around an otherwise rigid and inflexible approach when using standalone energy simulation programs. For further discussions on this, see Sahlin *et al.* (2004), Chow *et al.* (1997), Trčka and Hensen (2010) and Bertagnolio and Lebrun (2008). For examples of equation-based methods see F_Chart (2011), Modelica (2010) and SPARK (2010).

When choosing a modelling method for plant and control modelling complexity and rigour are to be traded with computational cost (i.e. computer processing times). Since this affects time and money both in terms of data preparation as well as in terms of the turnaround times due to computer processing, busy practitioners require to exercise judgement when making a choice of modelling method which usually amounts to selecting the least complex (and rigorous) approach that will deliver the level of output detail, precision and accuracy needed to meet a given modelling objective. In most modelling applications, it is the level of rigour associated with plant and control modelling that will dominate computation cost rather than the modelling of the building envelope itself.

Rigour in relation to modelling plant and control has a strong association with the simulation time horizon over which the modelling is to be conducted – indeed the two considerations relate to one another inversely. This, in turn, has a clear association with the problem-solving application. Some examples can be found in Table 18.1.

Table 18.1 Some typical applications for plant and control modelling

Time horizon	Typical applications	Complexity
Long (seasons to years)	• Seasonal energy use • Seasonal carbon emissions • Control strategy • Building zoning • Summer overheating and air conditioning feasibility • Limited optimisation studies	Low
Moderate (months to seasons)	• Plant selection (strategic) • Plant sizing • Selection of working fluids • Adaptive comfort • Primary plant performance • Weather data impacts • Need for humidity control • Comparative plant performance • Optimisation studies	Moderate to high
Low (seconds to days)	• Control design and stability • 'Smart' controller design • Decision-making algorithms • Optimal design and response • Detailed plant response analysis • Thermal storage system design • Critical selection of working fluids • Real-time analysis and system status • System fault detection and diagnosis • Artificial intelligence applications	High to very high

Strategies for modelling plant and control

Not surprisingly, three strategic approaches are available for modelling plant and control that map onto the three sets of applications in Table 18.1. In practice, many commercially-available and freeware computer codes that enable plant modelling involve a degree of hybridisation between at least two of the methods. Table 18.2 summarises the three possibilities with comments on very typical computational cost based on today's personal computer hardware. Each of the methods will be explored in detail in the subsequent sections of this chapter.

Table 18.2 Some typical applications for plant and control modelling

Method	*Typical features*		*Typical computational cost*
Balanced energy	1.	Participating building is modelled rigorously/dynamically.	Seconds to a few minutes (*)
	2.	Un-modelled plant.	
	3.	Perfect control set point tracking imposed.	
	4.	Constant plant performance metrics imposed.	
Quasi-steady-state modelling	1.	Participating building is modelled rigorously/dynamically.	Minutes up to one or two hours (*)
	2.	Plant modelled using algebraic energy and mass balances.	
	3.	Plant capacity proportional to control system demands.	
	4.	Makers 'equation-fit' plant models or look-up tables for plant performance metrics.	
Fully dynamic modelling	1.	Any participating building may, in some instances, use a simple steady-state model.	Minutes up to several hours or days (*)
	2.	Plant modelled using differential equations.	
	3.	Plant capacity adjusted by control algorithm.	
	4.	Plant performance metrics determined by the model.	

*Broadly, the computer elapse time needed to solve a moderately complex problem. For balanced energy and quasi-steady-state methods this will mainly depend on the number of participating building zones. Fully dynamic modelling is usually either at plant level only or involving coupling with a simplified single zone building.

Plant modelling using energy balance method

The plant is not modelled in this approach, through the building is rigorously modelled using dynamic methods as described elsewhere in this book. With target heating and cooling (as

relevant) control set points defined for each zone of the building, it is simply assumed that the plant always tries to maintain the set point at all times when the plant is made available up to the limit of the pre-defined plant capacity. When the plant first switched on, the maximum capacity of the secondary plant is imposed on the building rooms and zones and propagated back to the primary plant. The zone temperatures will rise (winter) and usually fall if air-conditioned (summer) until it reaches set point and then be maintained there. Thus, the plant capacity to meet the set point in these conditions is determined by room/zone energy balances.

The room/zone energy balance is given by Eqn. 18.1.

$$V \rho_a c_a \frac{dT_{ai}}{dt} = \sum_{i=1}^{N} A_i h_i \left(T_{s,i} - T_{ai} \right) + m_{infil} c_a \left(T_{ao} - T_{ai} \right) + q_{cas} + q_{plant} \qquad (18.1)$$

Thus, at all times when the plant is made available and the room/zone temperature, T_{ai}, is above (cooling) or below (heating) the pre-defined set point value, the maximum (rated) capacity of the plant, q_{plant}, is added (heating) or deducted (cooling) and T_{ai} free-floats towards its target value. When it gets there, it is held at its set point value and Eqn. 18.1 is now used to calculate a balancing value of q_{plant} (less than or equal to its rated value) to maintain T_{ai}. These calculates are repeated at each time interval appropriate to the building simulation and, over time, q_{plant} is integrated to give energy use in kWh. When the plant is not offered, its value is set at zero and Eqn. 18.1 is then used to calculate a free-float value of T_{ai}. Of course, by this method, it is possible for q_{plant} to be held at its rated value indefinitely so long as T_{ai} has not reached target and this situation will provide evidence of under-sized plant. So, some useful results can be determined by a modelling approach of this kind though its utility is limited as far as the analysis of plant behaviour is concerned.

Example 18.1 energy balance method

A room measures 5m × 5m × 3m (high). All room surfaces are at a steady 18°C and have a convection coefficient of 8Wm⁻²K⁻¹ there is a constant infiltration air change rate of 0.5h⁻¹ and there is a constant casual heat gain to the room of 10Wm⁻² of floor area. The density and specific heat capacity of the room air are 1.2kgm⁻³ and 1005Jkg⁻¹K⁻¹ respectively.

a) What will be the plant load to maintain the room at 20°C when the external air temperature is 0°C?
b) What will the room temperature settle at when the plant (and casual heat gains) are off, the room surface temperature is at a steady 14°C and all other conditions are unchanged?
c) In summer the temperature of all room surfaces on a particular day is at a steady 28°C. What will be the plant load to maintain the room at 24°C when the external air temperature is 20°C and all other conditions remain the same?

Solution:

At a maintained (i.e. steady-state) room temperature, the LHS of Eqn. 18.1 will be zero.

Total area of room surfaces: $4 \times 5 \times 3 + 2 \times 5 \times 5 = 110m^2$

Room volume: $5 \times 5 \times 3 = 75m^2$

$\therefore m_{\text{infil}} = 1.2 \times 75 \times 0.5 / 3600 = 0.0125 \text{kgs}^{-1}$

Casual heat gain: $q_{\text{cas}} = 10 \times 5 \times 5 = 250\text{W}$

Part (a) – the plant load can be calculated as follows:

$0 = 8 \times 110 \times (18 - 20) + 1005 \times 0.0125 \times (0 - 20) + 250 + q_{\text{plant}}$

from which $q_{\text{plant}} = 1761\text{W}$

Part (b) – a settled room temperature implies a steady-state so the LHS of Eqn. 18.1 is again zero. q_{plant} (and q_{cas}) are now zero so Eqn. 18.1 can now be used to find T_{ai}:

$0 = 8 \times 110 \times (14 - T_{\text{ai}}) + 1005 \times 0.0125 \times (0 - T_{\text{ai}}) + 0 + 0$

from which $T_{\text{ai}} = 13.8^{\circ}\text{C}$

Part (c) the plant load is obtained for these conditions:

$0 = 8 \times 110 \times (28 - 24) + 1005 \times 0.0125 \times (20 - 24) + 250 + q_{\text{plant}}$

from which $q_{\text{plant}} = -3470\text{W}$ (i.e. negative sign implies a cooling plant load).

End of solution.

The above is a somewhat trivial example because all of the boundary variables will tend to vary all the time but it does illustrate the simplicity of this approach to plant modelling.

Steady-state modelling

Greater rigour and modelling utility than is possible using balanced energy modelling can be achieved when each plant component is given a functional relationship in which the output variables of interest are made a function of its input variables and certain physical parameters. It is appealing to note that, in many instances of plant modelling, the rates of change of plant components are much faster than those of the building envelope. This means that where the building envelope can be adequately modelled using time intervals that are larger than the response time of the plant then the plant can be treated as if it were a steady-state problem. Such an approach is sometimes called quasi-steady-state modelling. Many familiar and reliable methods of modelling can then be used.

Control Functions

The simplest approach is the use of control functions which assumes that the plant will respond to control signals in a perfectly linear manner. As an illustration consider the control of heating and cooling functions in a room or zone of a building. A control function diagram is shown in Figure 18.1 which is based on a two-channel control governing heating and cooling. There is a heating control set point, $T_{\text{H-SP}}$, and a cooling set point, $T_{\text{C-SP}}$, and there are corresponding proportional bands, *HCB*, *CCB*, which define the range of the control variable for which the output of the system is directly proportional. If the control system is perfectly linearized, then

the signal forming the vertical axis will be directly proportional to plant output. With this method then, the control variable (e.g. room or zone temperature) is not maintained constant but can float either side of a target set point value. This gives a more realistic prediction of plant response than is afforded by the balanced energy approach.

It is possible to define a formal expression for the heating and cooling plant outputs to meet the conditions defined in the control function diagram (eqns. 18.2, 18.3).

$$q_{\text{H}}(t) = \min\left(q_{\text{H-design}}, \max\left(0, q_{\text{H-design}} \times \left(\frac{T_{\text{H-SP}} + HCB/2 - T_{\text{ai}}(t)}{HCB} \right) \right) \right) \qquad (18.2)$$

$$q_{\text{C}}(t) = \min\left(q_{\text{C-design}}, \max\left(0, q_{\text{C-design}} \times \left(\frac{T_{\text{ai}}(t) - T_{\text{C-SP}} + CCB/2}{CCB} \right) \right) \right) \qquad (18.3)$$

Example 18.2 control functions

Suppose that the control function diagram of Figure 18.1 is used to control heating and air conditioning terminals in a room with design capacities matching the values obtained in the previous example (i.e. 1761W heating and 3470W cooling). The heating set point is 20ºC and the cooling set point is 24ºC. Both proportional bands are 2K. What will be the plant status when prevailing room temperatures are, a) 19.3ºC and, b) 23.8ºC?

Solution:

a) The heating control range is 20ºC ± 2/2 = 19-21ºC. So a prevailing temperature of 19.3ºC is within the heating control band and the cooling will therefore be off. The heat output of the plant will be:

$$q_{\text{H}}(t) = \min\left(1761, \max\left(0, 1761 \times \left(\frac{20 + 2/2 - 19.3}{2} \right) \right) \right) = 1497\text{W}$$

b) The cooling control range is 24ºC ± 2/2 = 23-25ºC. A prevailing temperature of 23.8ºC is within the cooling control band so the heating will now be off. The cooling load on the plant will, therefore, be:

$$q_{\text{C}}(t) = \min\left(3470, \max\left(0, 3470 \times \left(\frac{23.8 - 24 + 2/2}{2} \right) \right) \right) = 1388\text{W}$$

End of solution.
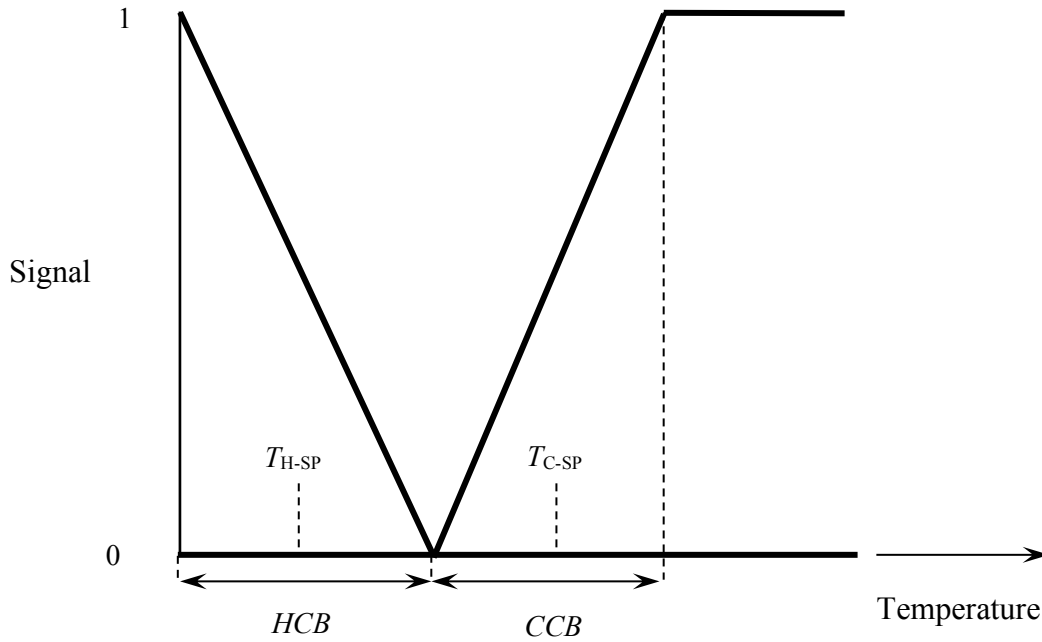
Figure 18.1 Typical control function diagram for room heating and cooling.

Steady-state Theory

For greater modelling precision and detail, the plant can be described using established steady-state theory provided that the central assumption of quasi-steady-state modelling applies (i.e. plant disturbance response times within one building fabric modelling sampling interval). An example of this for heat transfer processes is the use of the effectiveness method (Kays and London, 1964), in which the effectiveness is defined by eqns. 18.4 − 18.8.

$$E(t) = \begin{cases} \dfrac{T_{co}(t) - T_{ci}(t)}{T_{hi}(t) - T_{ci}(t)} & \left(m_h(t)c_h > m_c(t)c_c\right) \\[4mm] \dfrac{T_{hi}(t) - T_{ho}(t)}{T_{hi}(t) - T_{ci}(t)} & \left(m_h(t)c_h < m_c(t)c_c\right) \end{cases} \qquad (18.4)$$

In Eqn. 18.4 the heat exchange effectiveness at some point in time, *t*, for processes undergoing sensible counter-flow heat transfer for example, is given by Eqn. 18.5.

$$E(t) = \frac{1 - \exp[-NTU(t)(1 - C(t))]}{1 - C(t)\exp[-NTU(t)(1 - C(t))]} \qquad (18.5)$$

Alternatively, where one fluid is undergoing isothermal boiling or condensing heat transfer, Eqn. 18.6 may be used.

$$E(t) = 1 - \exp\left(-NTU(t)\right) \tag{18.6}$$

In the above, *NTU* is the number of (heat) transfer units (Eqn. 18.7) and *C* is the heat exchanger capacity ratio (Eqn. 18.8).

$$NTU(t) = \frac{AU}{\min\left(m_c(t)c_c, m_h(t)c_h\right)} \tag{18.7}$$

$$C(t) = \frac{\min\left(m_c(t)c_c, m_h(t)c_h\right)}{\max\left(m_c(t)c_c, m_h(t)c_h\right)} \tag{18.8}$$

Example 18.3 steady-state analysis

The condenser of a heat pump has an overall *AU* value of 35kWK^{-1} and serves a hot water space heating system with a circulating mass flow rate of 5kgs^{-1}. The mass flow rate remains constant at all part-load conditions and the heating water temperature range at design conditions is 10K. Heating control is achieved by varying the flow temperature to the heating system using a schedule which has a heating water temperature range of 30 to 55°C (design) corresponding to an external air temperature range of –3°C (design) to 15°C. On a particular day the external air temperature is 5°C at the start of the heating cycle and rises to 10°C by the end of the heating cycle. Find the range of heat pump condensing temperatures. (Take the specific heat capacity of water to be 4.2kJkg^{-1}K^{-1}.)

Solution:

A schedule allows the controlled variable set point to be adjusted with respect to some other reference variable. Here, the heating water set point at the heat pump condenser outlet is scheduled with respect to the external air temperature as shown in Figure 18.2. This can be interpreted as a linear equation with a negative gradient of 15K / 18K and an intersection at 0°C external temperature of 52.5°C heating water temperature.

When the heating first switches on, the external air temperature is 5°C and so the schedule will fix the required heating flow water temperature at: 52.5 – 15 × 5 / 18 = 48.3°C.

Because the 'hot' side of the condenser involves a vapour condensing nominally isothermally, the specific heat of this vapour, d*h* / d*t* $\rightarrow \infty$ so $m_c \times c_c = 5 \times 4.2 = 21$kJK^{-1} is the smaller of the two heat capacities which results in: *NTU* = 35 / 21 = 1.667.

The relevant calculation for the effectiveness will be Eqn. 18.6 since this heat exchanger involved condensing heat transfer.

$\therefore E$ (5°C) = 1 – exp (– 1.667) = 0.811

The water temperature difference across the condenser at these conditions can be calculated by assuming that it varies in proportion to the scheduled load since the heating water mass flow rate is constant. Thus, the present water temperature range will be $10 \times (15 - 5) / (15 - -3) = 5.56$K. So, the present heating water return temperature will be $48.3 - 5.56 = 42.74$ºC.

Applying Eqn. 18.4 in which $m_h \times c_h > m_c \times c_c$: $0.811 = 5.56 / (T_{hi}(t) - 42.74)$, from which the condensing temperature (i.e. $T_{hi}(t)$) at these conditions is found to be 49.6ºC.

Re-assessing for the conditions later in the day which the external air temperature has become 10ºC the following are obtained…

Updated heating water flow temperature: 44.17ºC.

NTU and, hence, *E* are unchanged.

Updated heating water inlet temperature: 41.39ºC.

Revised condensing temperature: 44.8ºC.
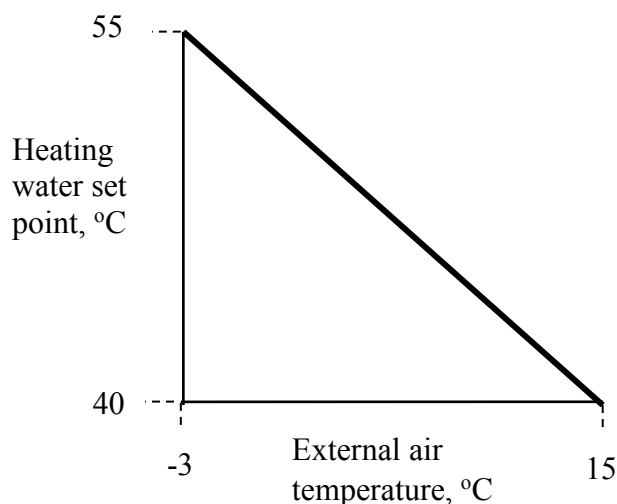
Figure 18.2 Heating schedule (used in Example 18.3).

Greater detail (and precision) in modelling information is evident in this method. The prediction of heat pump condensing temperatures means that the heat pump condensing pressure can be obtained. If the evaporating temperature (and, hence, compressor suction pressure) can be obtained by a similar method to that illustrated in this example then the pressure ratio can be used to predict part-load performance of the compressor itself leading to an accurate prediction of heat pump performance and power consumption. (In a complete building simulation, the load on the heating system would be known from other variables so the rather crude assumption of heating demand variation used in the above illustration would not be necessary.)

End of solution.

Though the above method works well for inflow heat exchangers, room-based heat exchangers such as radiator-convectors (i.e. 'baseboard' heaters) with mixed mode radiant and convective heat transfer on the room side of the heat exchanger require a different approach. A simple but adequate prediction of room emitter output can be obtained following the methods in BS EN 442-3 (BSI, 2008a) and the Hydronics Institute (1990) as summarised here in Eqn. 18.9.

$$q(t) = K\left(T_{\mathrm{m}}(t) - T_{\mathrm{r}}(t)\right)^n \tag{18.9}$$

Catalogue-fit Modelling

The availability of comprehensive manufacturers' catalogue data describing the performance of certain types of plant can offer a simple and convenient route to robust plant modelling – so-called 'catalogue-fit' models. The more comprehensive examples of data can be found for certain types of primary plant – in particular heat pumps and chillers. Because these plants can be both complex and difficult to fully parameterise for the purpose of modelling from first principles catalogue-fitted models have considerable appeal. The comprehensiveness of the data arises from the international standards that manufacturers are required to report their product performances to – examples for heat pumps and air conditioners include BS EN 14825 in Europe (BSI, 2008b) and the ARI standards in the USA (ARI, 1998).

The common structure is a polynomial relating an output variable such as a performance metric (e.g. coefficient of performance, *CoP*) to a single input such as source or sink temperature as depicted in Eqn. 18.10.

$$CoP(t) = a_0 + a_1 T(t) + a_2 T(t)^2 + \dots + a_m T(t)^m \tag{18.10}$$

in which $a_0 \dots a_{\mathrm{m}}$ are regression fitting constants.

For more detailed models, the bi-quadratic structure given in Eqn. 18.11 may be used. Here, an output variable, $z(x,y)$, is fitted to two or more independent variables using a multiple regression fitting method ($a_0 \dots a_2$ and $b_0 \dots b_2$ are fitting constants).

$$z(x, y) = \left(a_0 + a_1 x + a_2 x^2\right) \times \left(b_0 + b_1 y + b_2 y^2\right) \tag{18.11}$$

As an example, Yik *et al.* (2012) offer the following relationship for chiller power demand, *w*, as a function of air conditioning load, *q*, and condenser air or water inlet temperature for oil-free centrifugal chillers (Eqn. 18.12). The fitting constants can be found in Table 18.3.

$$W(t) = a_0 + a_1 q_{\mathrm{c}}(t) + a_2 q_{\mathrm{c}}(t)^2 + a_3 T_{\mathrm{i}}(t) + a_4 T_{\mathrm{i}}(t)^2 + a_5 q_{\mathrm{c}}(t) T_{\mathrm{i}}(t) + \dots$$
$$a_6 q_{\mathrm{c}}(t)^2 T_{\mathrm{i}}(t) + a_7 q_{\mathrm{c}}(t) T_{\mathrm{i}}(t)^2 + a_8 q_{\mathrm{c}}(t)^2 T_{\mathrm{i}}(t)^2 \tag{18.12}$$

Table 18.3 Fitting constants for the catalogue-fit example model in Eqn. 18.12 (Yik et al., 2012).

Constant	Air-cooled	Water-cooled
a_0	0.007000	0.048346
a_1	-0.008249	0.184133
a_2	0.461093	0.201874
a_3	-0.0005403	-0.002417
a_4	0.00002641	0.00006864
a_5	0.018328	0.002683
a_6	-0.019843	-0.001912
a_7	-0.0001393	0.000432
a_8	0.0006012	0.0001234

Another common application for catalogue-fit type models is for use in modelling fans and pumps. Third-order polynomial fitting usually gives a very good accuracy and representation. For example, fan/pump pressure from inlet volume flow rate (Eqn. 18.13) and fan/pump power consumption from inlet volume flow rate (Eqn. 18.14). Again $a_0...a_3$ and $b_0...b_3$ are regression fitting constants and P_0, V_0 and W_0 are reference values of fan/pump pressure, inlet volume flow rate and power respectively.

$$P(t) = a_0 + a_1\left(\frac{P_0}{V_0}\right)V(t) + a_2\left(\frac{P_0}{V_0^2}\right)V(t)^2 + a_3\left(\frac{P_0}{V_0^3}\right)V(t)^3 \tag{18.13}$$

$$W(t) = b_0 + b_1\left(\frac{W_0}{V_0}\right)V(t) + b_2\left(\frac{W_0}{V_0^2}\right)V(t)^2 + b_3\left(\frac{W_0}{V_0^3}\right)V(t)^3 \tag{18.14}$$

In common with examples such as Eqn. 18.13, these equations merely need to be solved at building modelling time intervals to provide an updated value of plant status and output. One criticism of this approach is that the manufacturers' data upon which these component models are based are themselves usually based on a predictive model rather than comprehensive test data. In effect, a model is being fitted to another model. However, the manufacturers' data has to be accurate and robust in order to comply with the standards to which they relate (not to mention the risk of litigation). A further criticism is that these models are only suitable strictly within the ranges of the data to which they are fitted. This is a matter for the user/modeller to take on board.

Dynamic-state modelling

For a more rigorous and detailed treatment of modelling building plant, recognise that variables change in reality with both time and spatial position. In practice the rates of change of variables describing plant behaviour with respect to time tend to be much faster than similar variables describing behaviour in the fabric of buildings. This results in a wide range of time rates-of-change when all of the equations for both building fabric (as described elsewhere in this book) and plant are put together – a so-called 'stiff' system of equations. Stiff models are often tricky to solve and require high computational power (often alleviated through variable-step solvers) so ideas for simplifying the problem can be helpful. For example, relaxing the plant modelling technique to quasi-steady-state as described in the previous Section. Alternatively, when solving problems over short time horizons, the building model can be relaxed to a fixed boundary or steady-state problem allowing an efficient focus to be placed on the plant. As far as spatial rates of change are concerned, this will tend to be of greatest interest with larger distributed systems. For example, large complex heat exchangers, underfloor heating, chilled ceilings, etc. For a rigorous approach in which both time and spatial position play roles as independent variables, problem descriptions require to resort to partial differential equations (PDEs).

Linear Systems of Equations

In many cases, it will be possible to restrict the spatial domain to one dimension only – usually that along the flow path thus assuming perfect lateral mixing. For example, a room-based heating operation using hot water as a dynamic spatially-distributed problem can be described by Eqn. 18.15.

$$\frac{C_{\text{hm}}}{x} \frac{\partial T}{\partial t} = m_{\text{h}} c_{\text{h}} \frac{\partial T}{\partial x} - \frac{AU}{x} \left(T - T_{\text{r}} \right) \tag{18.15}$$

For linear time-invariant problems in which model parameters remain constant (i.e. C_{hm}, m_{h}, c_{h}, AU are constant) a convenient approach is to discretise the problem spatially which results in a set of ordinary differential equations in which time is the only independent variable. The advantage of this approach is that a wide variety of numerical integration algorithms can be used to solve the resulting equation set. By dividing the spatial domain, x, into N equally sized zones each of width, Δx, a set of N ordinary differential equations will arise. The partially-discretised form of Eqn. 18.15 for the nth zone can be expressed as Eqn. 18.16.

$$\frac{C_{\text{hm}}}{N\Delta x} \frac{\text{d}T_n}{\text{d}t} = \frac{m_{\text{h}} c_{\text{h}}}{\Delta x} \left(T_{n-1} - T_n \right) - \frac{AU}{N\Delta x} \left(T_n - T_{\text{r}} \right) \tag{18.16}$$

which reduces to Eqn. 18.17.

$$\frac{dT_n}{dt} = \alpha\left(T_{n-1} - T_n\right) - \beta\left(T_n - T_r\right) \tag{18.17}$$

in which: $\alpha = \dfrac{Nm_h c_h}{C_{hm}}$ and $\beta = \dfrac{AU}{C_{hm}}$, where C_{hm} is the overall thermal capacity of the water occupying the emitter and the material forming the heat transfer surface of the emitter. At the inlet zone of the emitter, T_{n-1} is replaced with the inlet water temperature. As a set of N ordinary differential equations will arise, a matrix differential equation can be written (Eqn. 18.18).

$$\mathbf{T} = \mathbf{A}x + \mathbf{B}u \tag{18.18}$$

where $\mathbf{T}$ is an $N \times 1$ vector of derivatives, $\mathbf{A}$ is an $N \times N$ matrix of coefficients, x is an $N \times 1$ vector of input variables, $\mathbf{B}$ is an $N \times 2$ matrix of boundary variable coefficients. (There are two boundary variables – the emitter inlet water temperature and the room air temperature.) $\mathbf{u}$ is a 2×1 vector of boundary variable values.

An expansion of Eqn. 18.18 is given in Eqn. 18.19. Note that the $\mathbf{A}$ matrix of coefficients is diagonally dominant.

$$\begin{bmatrix} T_n \\ T_{n+1} \\ . \\ . \\ . \\ T_N \end{bmatrix} = \begin{bmatrix} -(\alpha+\beta) & 0 & . & . & . & 0 \\ \alpha & -(\alpha+\beta) & 0 & . & . & 0 \\ 0 & \alpha & -(\alpha+\beta) & 0 & . & 0 \\ 0 & . & . & . & . & 0 \\ 0 & . & . & . & . & 0 \\ 0 & . & . & 0 & \alpha & -(\alpha+\beta) \end{bmatrix} \times \ldots$$

$$\tag{18.19}$$

$$\ldots \begin{bmatrix} T_n \\ T_{n+1} \\ . \\ . \\ . \\ T_N \end{bmatrix} + \begin{bmatrix} \alpha & \beta \\ 0 & \beta \\ . & . \\ . & . \\ . & . \\ 0 & \beta \end{bmatrix} \times \begin{bmatrix} T_{inlet} \\ T_r \end{bmatrix}$$

A key issue is the choice of the number of modelling zones, N, which will tend to vary from application to application. Further consideration will be given to this in an application case study in the next Section and for a detailed treatment of this applied to room heat emitters, see Fong *et al.* (2015).

Nonlinear Systems of Equations

An inspection of Eqn. 18.16 shows two obvious sources of nonlinearity. First, if the heating system mass flow rate, m_h, is not constant then a product of two variables arises (mass flow rate and temperature). In fact, the variation of heating water mass flow rate is a common method of plant capacity control so this will arise in many practical modelling applications. Second, a sophisticated plant model is likely to incorporate a function for the calculation of the heat transfer coefficient, AU, which is likely to vary independent of time as a function of other variables in the model. These nonlinearities mean that a more flexible approach will be needed for the treatment of Eqn. 18.16. This is afforded by fully discretising in both time and space and solving the resulting algebraic equation set iteratively. Re-casting Eqn. 18.16 with the time term discretised using a backward-in-time method and simplifying results in Eqn. 18.20.

$$T_{n,t} = \frac{C_{hm}T_{n,t-\Delta t} + \Delta t N m_h c_h T_{n-1,t} + \Delta t A U T_{r,t}}{C_{hm} + \Delta t N m_h c_h + \Delta t A U} \qquad (18.20)$$

An iterative loop must be visited at each time instant to solve an equation such as 18.20. This is because, though the temperatures along the heat exchanger in each zone are known at the previous time instant they are not known at the current time instant. A glance at Eqn. 18.20 shows temperatures at the current time instant on both sides of the equation ($T_{n,t}$ and $T_{n-1,t}$) and so an iterative approach is used. A common method is to use a Gauss-Seidel scheme (also known as successive displacement or successive substitution). This method works as follows with reference to Eqn. 18.20.

Step 1 – at the current time instant, t, $T_{n...N,t-\Delta t}$ will be known and $T_{r,t}$ will be supplied from other model equations. (If m_h and/or AU are time-variant; $m_{h,t}$, AU_t, they too will be updated from other model equations.)

Step 2 – visit each zone, n, and update $T_{n,t}$ using Eqn. 18.20 holding $T_{n...N,t-\Delta t}$ constant. This will results in an updated set of values $T_{n...N,t}$. Store the results.

Step 3 – check the updated values values $T_{n...N,t}$ with the previously stored values. If all values are within an acceptable tolerance of the previously stored values at each zone location, replace $T_{n...N,t-\Delta t}$ with $T_{n...N,t}$, advance time by Δt and continue. If not, go to Step 2.

Modelling case studies in plant and control

In this Section, consideration will be given to several contrasting plant modelling case studies making use of some of the theories described in the foregoing sections. The first of these will deal with the question of spatial discretisation in plant modelling. The second will consider a primary plant application involving a heat pump coupled to a thermal store. The third case study will consider the modelling of a simple feedback control loop applied to air heating and cooling plant.

Case study 1: Heat emitter model discretisation analysis

In this case study the influence of the number of modelling zones for a room emitter model of the type described in the previous Section will be considered. Consider a hot water heat emitter

with a design-rated capacity of 3kW when receiving hot water at 50°C (inlet) and 40°C outlet. The heat emitter is in a room space to be maintained at a nominal design temperature or 19°C when the external air temperature is –3°C. Compare the results of an arbitrary step change in heating water inlet temperature from 50°C to 60°C when the heat emitter is divided into 3 equally-sized modelling zones and 10 equally-sized modelling zones. Assume, for this exercise, that the room heat transfer can be described using a steady-state heat loss model.

Model used: Eqn. 18.17 interpreted as Eqn. 18.19.

Constants: α and β evaluated to be 4.524×10^{-3}s^{-1} and 5.75×10^{-4}s^{-1} respectively (3rd- order model) and α will be 1.508×10^{-2}s^{-1} for the 10th-order model (β unchanged).

Implementation: Use a Matlab-Simulink state-space block to implement Eqn. 18.19 with a Rosenbrock variable-step solver with the maximum step size fixed at 1s.

The model is given in Fig. 18.3 based on the step change in inlet hot water temperature occurring after 300s of initial steady-state plant response. Results are shown in Fig. 18.4 giving a comparison of the two room air temperature predictions (°C) and the two heat emitter output predictions (kW).

Conclusion: The room temperature settles approximately 1200s after the step change in inlet heating water temperature at 22.165°C for the 3rd-order model and 22.568°C using the 10th-order model. The final heat transfer values from the emitter are 3.43kW (3rd-order) and 3.49kW (10th-order). Though the final heat transfer values are very similar the higher order model is noted to take longer to settle. Though the difference between final temperatures appears relatively small (0.4K) this may be significant if the modelling application is used for control system simulation. This is because relatively small deviation in controlled variable value (i.e. likely to be room temperature in this case) can have a relatively high effect in control signal value. For a more detailed treatment of this subject, refer to Fong *et al.* (2015).
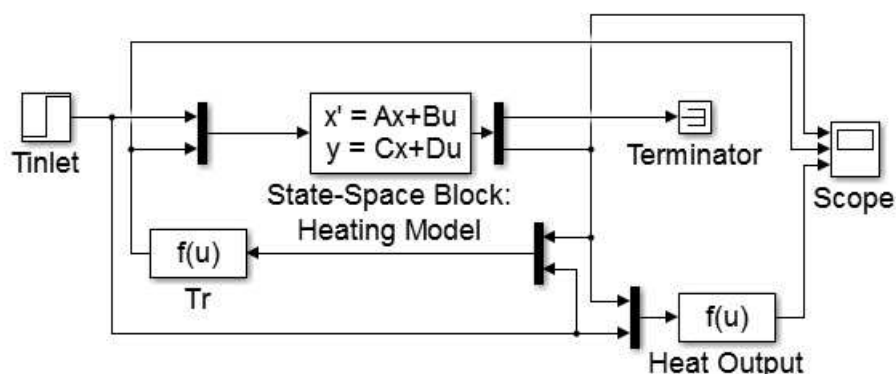

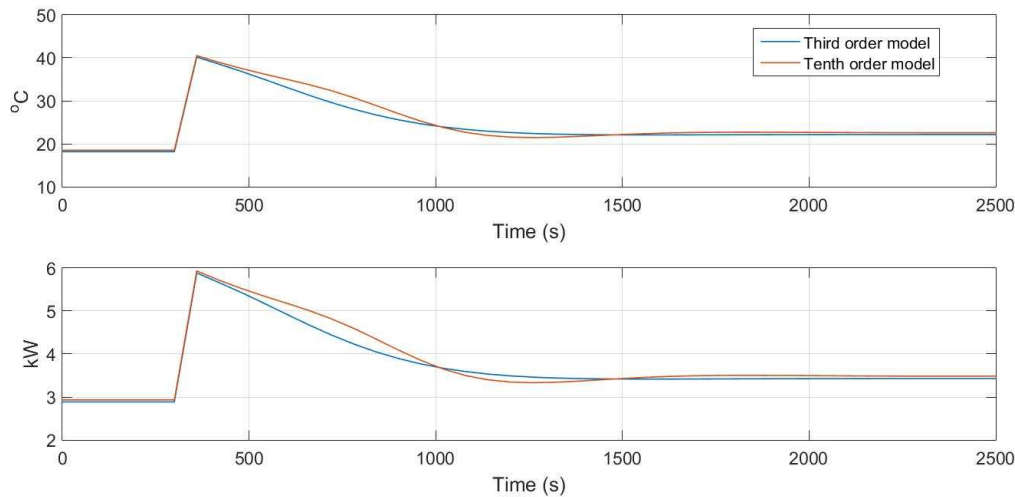*Figure 18.3 Information flow diagram for modelling case study 1.*

Figure 18.4 Results for case study 1.

Case study 2: Heat pump coupled to a hybrid thermal store

This case study considers the charge and discharge transient of a novel hybrid thermal store coupled to an air-source heat pump compared with a conventional water tank of the same volume. The thermal store consists of a salt-hydrate phase change material encapsulated in a set of stainless steel coils mounted in a water tank. The tank is designed so that it will fit into a standard kitchen under-bench module in a residential application. Full details of the modelling methods used and parameter and input data sets can be found in Underwood *et al.* (2018).

The model information flow diagram in this case is shown in Fig. 18.5. The input vector for the heat pump defines the external (source) air temperature, primary heating mass flow rate and the primary heating inlet water temperature to the heat pump. For the hybrid thermal store, the input vector comprises the primary heating inlet temperature and mass flow rate (from the heat pump), secondary heating system temperature and mass flow rate, ambient surrounding temperature and heating status switch (charging or discharging).

Two simulations are compared here – the hybrid thermal store and an alternative thermal store consisting of a water tank of the same volume. The simulations give the charge phase transient tank outlet temperature and the corresponding discharge phase temperature over one complete cycle. Results are plotted in Fig. 18.6 – the top graph showing the tank temperature during charge and discharge based on the two alternative tank types and the bottom graph showing the heat transfer discharged to the heating system (kW).

Results: Thermostat switching is evident during charge in the case of the hybrid thermal store. This is because the phase change material takes a finite time to fully melt which prompts several heat pump switching events. During discharge, it can be seen that the hybrid tank is able to hold a load of approximately 4kW for at least 2h whereas the conventional tank has fully discharged in this time. This is significant because a modern well-insulated house of medium size will have a space heating design load of, typically, 4-5kW in the UK (as an example). This means that the hybrid tank would be able to satisfy heating demand during the crucial electrical

grid-stress phase in later afternoon/early evening (Underwood *et al.,* 2018). The heating spike at the start of discharge is due to cold heating system water initially displacing warm tank water and once the heating system water catches up, this spike quickly settles down to the nominal heating system output value.
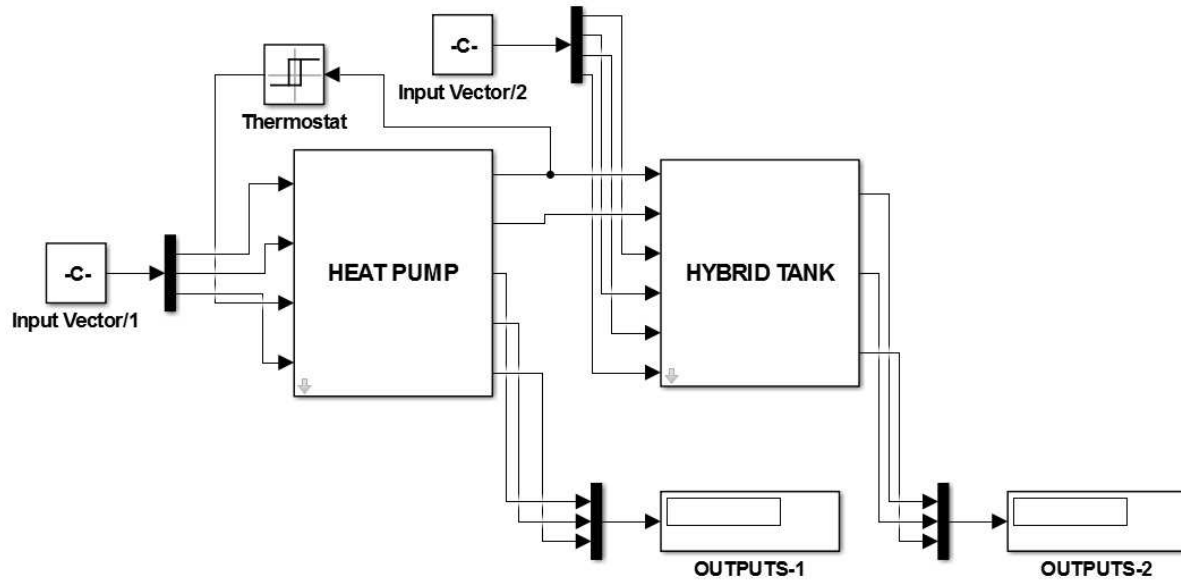
Figure 18.5 Information flow diagram for case study 2.
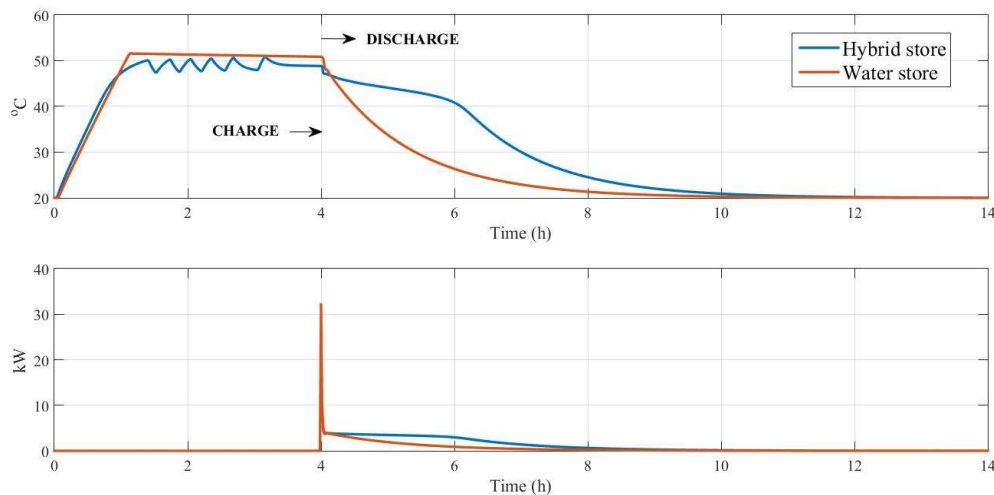
Figure 18.6. Results for case study 2.

Case study 3: Feedback control of an air cooling coil

In this final case study, consideration is given to a simplified treatment of the modelling of modulating feedback control of a common plant operation – that of air cooling using a chilled water cooling coil. The coil model is a 3rd-order model adopting a relatively simple contact factor approach (essentially, similar to the effectiveness concept described in Eqn. 18.6 but

with the coil sub-divided into three equally sized zones for dynamic modelling). The coil is modelled using the heat transfer correlations presented in Gomaa *et al.* (2002).

The coil is parameterised with a 1m^2 frontal area and an air face velocity of 2ms^{-1}. Chilled water at a constant 7°C is admitted at a design maximum flow rate of 3kgs^{-1}. The flow rate is varied in response to the error between the coil supply air outlet temperature and its set point value. The control signal is generated using a fixed gain value (which can be adjusted) – essentially proportional control. A saturation block is used to ensure that the chilled water mass flow rate cannot stray beyond its limits of 0,3kgs^{-1}. The complete model is shown in the information flow diagram of Fig. 18.7.

The plant was simulated over a 1h period using a uniform random number sequence for the disturbed inlet air temperature (varying in the range 18 – 28°C). The coil air outlet set point temperature was set to 12°C and, at 30-minutes, the set point was increased at 14°C in order to further explore the control tracking behaviour. Results are shown in Fig. 18.8.

Results: Using an arbitrary controller gain value of –1 (the negative sign to correct the control action for negative feedback) the control tracking is reasonably good especially when it is considered that the disturbance sequence is somewhat arbitrary for this illustration. This can be seen in graph 'A' of Fig. 18.8 (lower curve). It is also possible to see the increase in outlet air temperature starting at 30-minutes due to the increase in control set point. The increase in set point now means that the plant can operate more comfortably within its range (at the lower set point is was operating at close to its design capacity) and this is evidenced by a slightly lower variance in the controlled variable value as well as in chilled water flow rate (graph 'B' in Fig. 18.8) during which the flow rate spends less time at its upper limit value. Of course, this is far from optimal control and more sophisticated control methods could be considered but this case study illustrates the potential for plant modelling at a detailed level of enquiry.

For a more detailed treatment of the distributed modelling of cooling coils, refer to Underwood and Yik, Chapter 5 (2004), and for a more in-depth look at control systems and control system modelling for these types of application, refer to Underwood (1998).
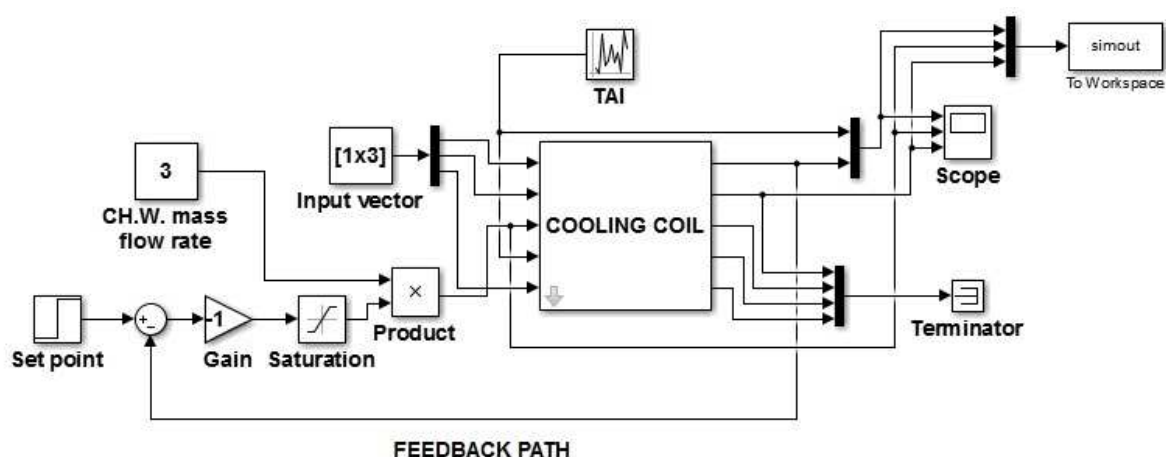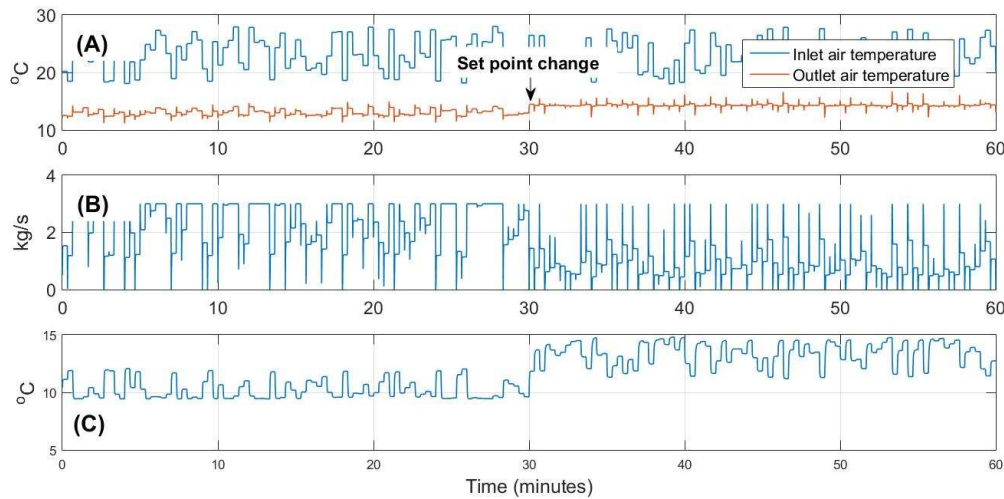

Figure 18.7. Information flow for case study 3.

A – Inlet and outlet air temperature; B – Chilled water mass flow rate; C – Chilled water outlet temperature

Figure 18.8. Results for case study 3.

Solar thermal collectors

A heat balance approach to modelling solar collectors needs to consider the incoming solar radiation normal to the solar collector and the losses to surroundings from the collector surfaces. In sunny but colds climates, the influence of the latter is particularly important. The solar radiation striking the surface-normal of the array will be reduced according to the transmissivity of the collector glass cover plate(s) and the absorptivity of the collector absorber surface before it reaches the heat transfer fluid. The losses from the collector on the other hand will be dependent of whether the absorber space is evacuated which reduces collector losses to, predominantly, skywards long-wave radiation. The energy balances about the collector fluid can be expressed with a modified form of Eqn. 18.17 as given in Eqn. 18.21.

$$\frac{\mathrm{d}T_n}{\mathrm{d}t} = \alpha\left(T_{n-1} - T_n\right) - \beta\left(T_n - T_a\right) + A_{\mathrm{abs}}S \tag{18.21}$$

in which A_{abs} is the absorber area and S is the solar radiation absorbed by the collector absorber plate (kWm^{-2} or Wm^{-2}). α and β can be defined in a similar manner as for Eqn. 18.17 with the exception that the AU component will represent the overall collector loss coefficient with its surroundings (kWK^{-1} or WK^{-1}). Note also that the fluid specific heat capacity in this case (i.e. in α) will not necessarily be for water but will depend on any antifreeze additive used.

For a simplified steady-state analysis of collector behaviour, Eqn. 18.21 can be reduced to Eqn. 18.22.

$$q_{\mathrm{utilised}} = A_{\mathrm{abs}}S - A_{\mathrm{col}}U_{\mathrm{L}}\left(\bar{T}_{\mathrm{cf}} - T_a\right) \tag{18.22}$$

(in which: $\bar{T}_{\mathrm{cf}} = (T_{\mathrm{cf,o}} + T_{\mathrm{cf,i}})/2$).

The overall heat utilisation from the collector can be obtained from Eqn. 18.23.

$$q_{\text{system}} = \max\left(0, m_{\text{cf}} c_{\text{cf}}\left(T_{\text{cf,o}} - T_{\text{cf,i}}\right)\right) \tag{18.23}$$

Related to this, an alternative modelling approach is to compare the actual heat delivered to the hot water system with the heat utilised by the collector had it been uniformly at a temperature equivalent to the inlet water temperature, $T_{\text{cf,i}}$. This defines a heat removal factor for the collector, F_R (Eqn. 18.24).

$$F_R = \frac{m_{\text{cf}} c_{\text{cf}}\left(T_{\text{cf,o}} - T_{\text{cf,i}}\right)}{A_{\text{abs}} S - A_{\text{col}} U_L (T_{\text{cf,i}} - T_a)} \tag{18.24}$$

It is now possible to define a collector thermal effectiveness, η_{col} (Eqn. 18.25).

$$\eta_{\text{col}} = \frac{q_{\text{system}}}{A_{\text{col}} \Sigma G} \tag{18.25}$$

in which $\Sigma G = G_{\text{dir,col}\_} + G_{\text{dif,col}} + G_{\text{gr,col}}$ where $G_{\text{dir,col}}$ is the direct solar radiation corrected to the normal of the solar collector, $G_{\text{dif,col}}$ is the diffuse solar radiation corrected to the normal of the solar collector and $G_{\text{gr,col}}$ is the surroundings-reflected solar radiation corrected to the normal of the solar collector. For the solar absorbed by the collector absorber (S in equations 18.21 and 18.22) the direct, diffuse and ground-reflected components require to be further corrected to account for the proportion of radiation at the collector surface-normal that is transmitted through the glass cover plate(s) of the collector and for the proportion of the transmitted radiation that is absorbed by the absorber plate – the so-called $\tau\alpha$ product. These corrections are given in Eqn. 18.26.

$$S = G_{\text{dir,col}} \tau\alpha_{\text{dir}} + G_{\text{dif,col}} \tau\alpha_{\text{dif}} + G_{\text{gr,col}} \tau\alpha_{\text{gr}} \tag{18.26}$$

The transmissivity of the essentially clear glass used for cover plates varies to some extent with the angle of incidence of the beam radiation and with the number of cover plates used. Two or more glass cover plates will reduce the transmitted solar radiation to the collector but will also reduce the top-loss component of the heat loss coefficient so a trade-off will be sought. Typically, the transmissivity will vary in the range 0.7 – 0.9 corresponding to 4 cover plates and 1 cover plate respectively. A larger number of cover plates is most likely to make sense in situations with long periods of excellent bright sunshine but with low ambient temperatures (i.e. certain high-altitude locations). Further details on the variation of $\tau\alpha$ can be found the ASHRAE Handbook (ASHRAE, 2016). The transmissivity will remain more or less constant for angles of solar incidence down to about 50º but will fall sharply at higher values of incidence angle. Corrections for angles of incidence off-normal can be obtained from Eqn. 18.27. b_0 in this equation is approximately –0.1 for single glass covers (Klein, 1975).

$$K_{\tau\alpha} = 1 + b_{\rm o}\left(\frac{1}{\cos\theta} - 1\right) \tag{18.27}$$

As to the absorber plate absorptivity, typical values of around 0.92 can be expected for plates with high-absorptivity coatings.

The overall thermal transmittance value, $U_{\rm L}$, in Eqn. 18.22 and Eqn. 18.24 will consist of a loss term at the top of the collector and, where relevant, the back and sides. The top loss will be dominant because it will also exhibit a significant contribution of skyward radiation loss besides convection. Wind flow will also play a strong role in the latter. For flat plate collectors, insulation at the back and edges of the collector will help to minimise these losses. Equations 18.28 and 18.29 can be used to account for these losses.

$$U_{\rm edge} = \frac{A_{\rm edge}}{A_{\rm col}} \times \left(R_{\rm so} + R_{\rm si} + \frac{x_{\rm edge}}{k_{\rm edge}}\right)^{-1} \tag{18.28}$$

$$U_{\rm back} = \left(R_{\rm so} + \frac{x_{\rm back}}{k_{\rm back}}\right)^{-1} \tag{18.29}$$

As to the dominant top loss *U*-value probably the most enduring loss model for flat plate collectors is due to Klein (1975) as given in Eqn. 18.30 and comprising a convective term and a longwave loss term.

$$U_{\rm top} = \left[\frac{N}{\dfrac{C}{\overline{T}_{\rm cf}}\times\left(\dfrac{\overline{T}_{\rm cf} - T_{\rm o}}{N + f}\right)^{e}} + \frac{1}{h_{\rm o}}\right]^{-1} + \frac{\sigma\times\left(\overline{T}_{\rm cf} + T_{\rm a}\right)\times\left(\overline{T}_{\rm cf}^{2} + T_{\rm a}^{2}\right)}{\left(\varepsilon_{\rm p} + 0.00591Nh_{\rm o}\right)^{-1} + \left(\dfrac{2N + f - 1 + 0.133\varepsilon_{\rm p}}{\varepsilon_{\rm g}}\right) - N} \tag{18.30}$$

in which:

$$f = \left(1 + 0.089h_{\rm o} - 0.1166h_{\rm o}\varepsilon_{\rm p}\right)\times\left(1 + 0.07866N\right)$$
$$C = 520\times\left(1 - 5.1\times10^{-5}\beta^{2}\right)$$
and,
$$e = 0.43\times\left(1 - 100/\overline{T}_{\rm cf}\right)$$

An overall loss coefficient for flat plate collectors is then obtained by summing the three terms (Eqn. 18.31).

$$U_{\rm L} = U_{\rm top} + U_{\rm edge} + U_{\rm back} \tag{18.31}$$

For evacuated tube collectors, convective losses are largely eliminated (other than surface convection from the outer glass surface depending on the amount of solar radiation absorbed in the glass but likely to be relatively minor) and so allowance for longwave loss only is generally sufficient. The complex geometries of these types of collectors means that it is usually preferable to obtain loss factors from test data which will usually be available from manufacturers.

Simulation Case Study 4: Solar Domestic Water Heating

This treatment of solar collectors is concluded with a case study consisting of an example simulation of a flat plate collector in two contrasting locations. In common with the other case studies considered in this chapter it should be noted that these examples are presented here as illustrations of the potential uses and applications of the plant modelling methods described in this Chapter rather than as robust and definitive solutions to the particular problems presented.

The model used is based on equations 18.21 – 18.31. Annual simulations are carried out with increasing collector array area in two contrasting climate locations – the hot city of Havana in Cuba (latitude 23°N) and the cooler city of Newcastle upon Tyne in the UK (latitude 54°N). The objective is to find how much of the hot water demand for a small family could be met by the array and at what overall annual efficiency. A new term is defined to support this – the demand removal factor, D_R, which is defined as the proportion of the hot water demand (including storage tank losses) that is met by the solar collector array. The information flow diagram for this system model is shown in Fig. 18.9. A break heat exchanger is included because, for the cold climate application, the collector array fluid would most likely contain an antifreeze solution for winter protection. Though this would not be strictly necessary in Havana, it was also included in these simulation for a consistent comparison (though it is unlikely to have had much impact on results). The demand processing block in Fig. 18.9 simulates (using a 10th-order model) a hot water storage tank with a cold water inlet and hot water outlet together with primary heat input coming from the break heat exchanger (i.e. solar collector array). The hot water demand is linked to the cold water and hot water inlet and outlet rates which are determined using one of a number of standard daily 'tapping cycles' which are assumed to repeat each day. The tapping cycle used in this case study is defined in BS EN 13203-2 (BSI, 2015). The 'medium' family demand set was used from this standard and fed from a 150-litre tank. Annual weather data appropriate for the two city locations was used.

Results: The results are presented in Fig. 18.10. The top graph ('A') shows an increasing proportion of demand removal with increasing collector area for both cities which is to be expected. The demand removal is almost fully achieved with the larger collector array size in the hot city of Havana though the rate of improvement slows considerably for array areas greater than 2-3m². For the cooler city of Newcastle, only 50% of the demand can be met with an array size of 6m² and there seems little point in further increases in size. Though the efficiency of the Havana collector array is higher than for Newcastle (where losses will be higher), both locations show reducing efficiency as the collector array size increases due to losses increasing at a higher rate than improvements in demand removal.
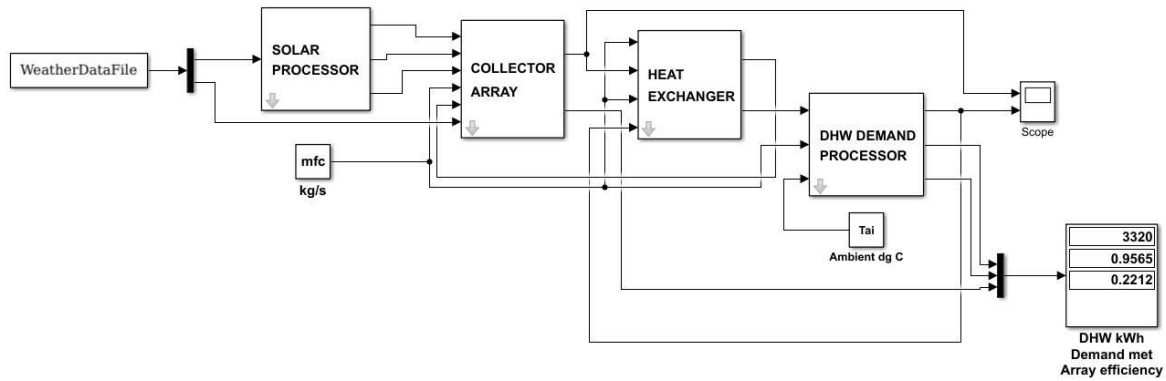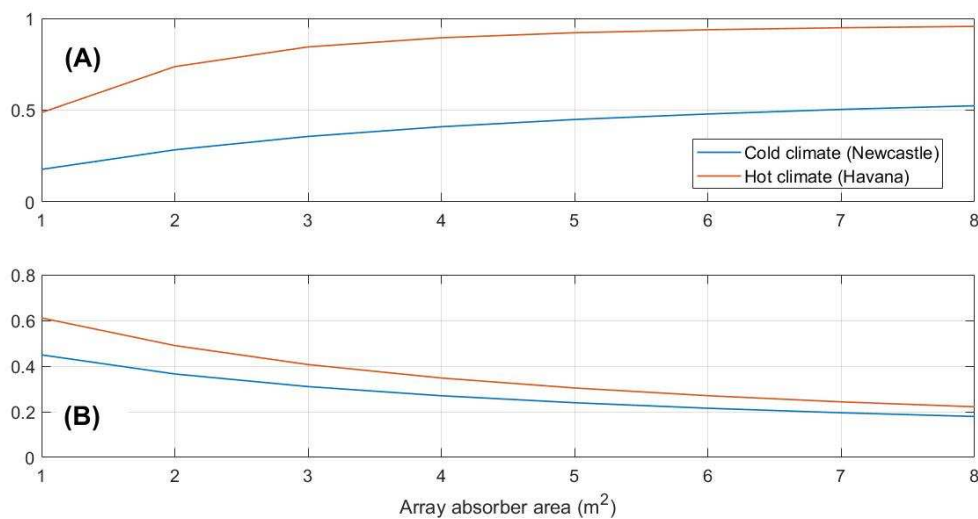
Figure 18.9 Information flow for solar water heating case study.

A – Demand removal factor; B – Collector efficiency

Figure 18.10 Results for solar water heating case study.

Solar photovoltaic systems

Solar photovoltaic (PV) systems are becoming increasingly important elements in building systems and impactful on building performance. Consequently, modelling of such systems has become increasingly important in predicting building performance and in designing both residential and non-residential buildings. Here we give an introduction to modelling such systems and present a model that has been used in a number of applications to represent realistic system behaviour.

The approach taken to modelling the performance of PV systems depends on the objectives of the modelling exercises and the level of detail of design information (parameter values) available. Whichever model is chosen we can express the electrical power delivered to the buildings (AC) system as a function of module area, A_{mod}, total solar irradiation on the module (panel) $G_{T,i}$ and functions of conversion efficiency as follows,

$$p_i = A_{mod} G_{T,i}\, \eta_{mod}(I_i, V_i, T_{c,i}, \dots)\, \eta_e(I_i, V_i, \dots) \qquad (18.32)$$

where η_{mod} is the efficiency of conversion of solar to DC electrical power of the module, and η_e accounts for the efficiency of conversion of DC to AC power in the combination of electrical system components often referred to as the 'balance of system' (principally the inverter efficiency). Both these efficiencies are functions of a number of other variables such as the instantaneous currents and voltages but also the thermal state of the panel and other environmental factors. The main difference between the available models is the degree of sophistication with which these functions are represented and also the length of integration of the power and solar fluxes. Possible calculation objectives and corresponding approaches include:

- assessment of PV contributions to the overall annual energy demands using synoptic climate data;
- simulation of the PV system assuming generic parameter values and fixed efficiencies;
- simulation of the renewable system using specific component data and hourly climate data;
- detailed simulation of the PV and electrical system components using short time-step data and explicit representation of the electrical/electronic sub-systems.

The ready availability of hourly climate data means that hourly simulation of PV systems that capture the primary climate-related factors effecting performance are feasible and implemented in many whole-building energy simulation tools. In such tools, prediction of incident solar fluxes and shading is straight forward (i.e. calculated by other models) and so the primary factors of interest – sensitivity to incident solar flux, coincident external temperatures and coincident demands – can be considered. Calculations of variation in performance on an hourly basis also allow tariff variations and import/export balances to be considered in the analysis.

At the early stages of building design – before specific PV products have been specified – it can be useful to make performance calculations with generic performance parameters and simple models. In this case the functions η_{mod} and η_e can be simply fixed values. An increased level of realism can be achieved by calculating efficiencies according to module current and voltage in particular solar, environmental and load conditions. Before describing the details of such approaches, it is necessary to define some characteristics of PV cells and modules.

In general, the current-voltage (*I-V*) characteristics of PV modules are very non-linear. At a given level of irradiation, the current is nearly constant over much of the operating voltage range and near the upper limit of the voltage range, the current drops dramatically. The power output (*p=IV*) correspondingly has a distinct peak towards the upper end of the voltage range. This is illustrated in Fig 18.11 Such characteristic curves can be defined by three pairs of *I* and *V* values at conditions of open circuit (zero current), short circuit (zero voltage) and maximum power: ($I_{oc}=0$, V_{oc}), (I_{sc}, $V_{sc}=0$), (I_{mp}, V_{mp}) as also shown in Fig 18.11 The relationship between V_{oc} is very close to linear in most cases as illustrated in Fig 18.12 (left). Data defining these three *I-V* points are published for standard conditions by module manufactures and are typically of the form shown in Table 18.4.

Some characteristics are sensitive to temperature and so power conversion efficiency is also ultimately sensitive to operating temperature. Open circuit voltage and short circuit current

are often taken to vary linearly with temperature about test conditions so that coefficients of variation (μ_{Voc} and μ_{Isc} respectively) with temperature are defined and published by manufacturers (for example, as in Table 18.4). Similarly a coefficient of variation of maximum power efficiency is given ($\mu_{p,mp}$) along with the value ($\eta_{mp,ref}$) at the reference conditions. These data are commonly used to derive other model parameters for simulation and design purposes.
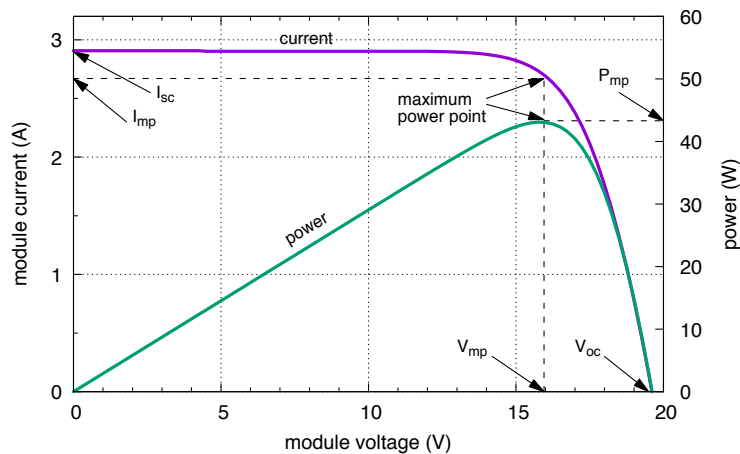

Figure 18.11 Typical characteristics of a photovoltaic module at standard test conditions.
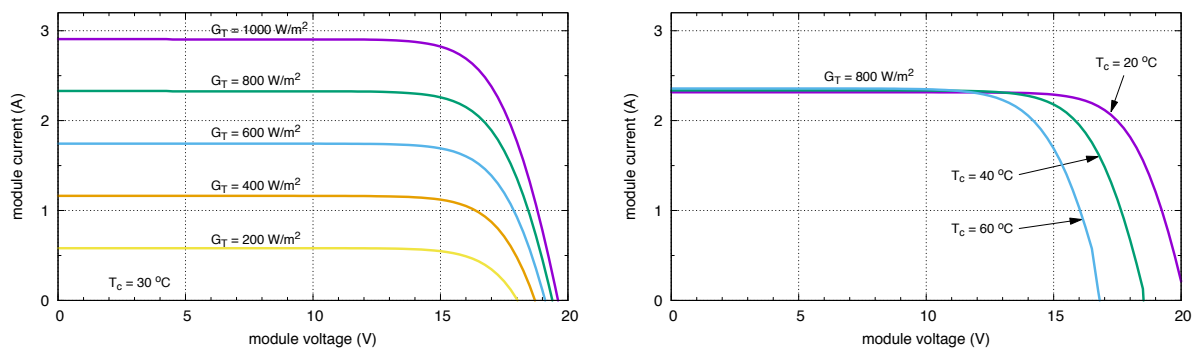
Figure 18.12 – Typical variation in photovoltaic module characteristics according to solar irradiation (left) and cell temperature (right).

Several models suitable for simulation and that use parameters derived primarily from manufactures data like that given in Table 18.4, have been derived based on conceptions of the module cells as equivalent diode circuits. These are typically based on a single-diode representation with either one or two resistances or two-diode representations as illustrated in Figure 18.13. In these representations, the stimulated photocurrent (I_{ph}) is offset by current through the diode (I_d) and leakage current (I_{sh}) through a parallel shunt resistance (R_{sh}) so that the net current (I) is given by,

$$I = I_{ph} - I_d - I_{sh} \tag{18.32}$$

Table 18.4. Performance electrical characteristics of a typical 0.5m² PV Panel. Data by BP Solar BP365U.

PV Panel Parameter	Value and Units
Maximum Power (p_{max})**	65W
Warranted minimum power	60W
Voltage at p_{max}	17.6V
Current at p_{max}	3.69A
Short circuit current	3.99A
Open circuit voltage	22.1V
Temperature coefficient of short circuit current (μ_{Isc})	(0.065±0.015)%/K
Temperature coefficient of open circuit voltage (μ_{Voc})	-(80±10)mV/K
Maximum Power Temperature coefficient ($\mu_{p,mp}$)	-(0.5±0.05)%/K
Nominal Operating Cell Temperature (NOCT)*	47±2°C
Module area: 36 cells 114mm square	0.468 m²
Efficiency at Standard Test Conditions (STC)** power ($\eta_{mp,ref}$)	0.139 (13.9%)

* Irradiance of 800 W/m², wind speed 1 m/s and air temperature of 20°C.

** Irradiance of 1000 W/m² at an AM1.5G solar spectrum and air temperature of 25°C.
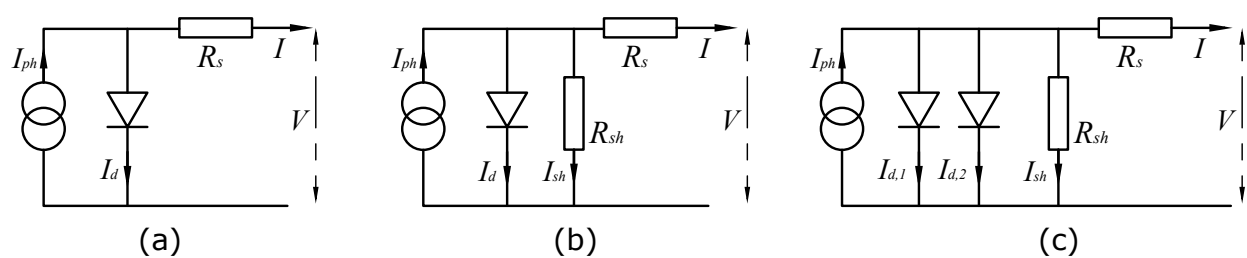
Figure 18.13 – Representations of photovoltaic cells based on single diode circuits without (a) and with (b) shunt resistances and two diodes (c).

The relationships between voltage and current for each of these terms can be substituted to give an overall voltage-current expression for the panel. For the diode the relationship is,

$$I_d = I_o \left[\exp\left(\frac{V + IR_s}{nV_T} \right) - 1 \right] \tag{18.33}$$

For the shunt resistance current,

$$I_{sh} = \frac{V + R_s I}{R_{sh}}$$

(18.34)

with:

$$V_T = \frac{kT_c}{q}$$

(18.35)

The overall *I-V* expression becomes,

$$I = I_{ph} - I_o\left[\exp\left(\frac{V + IR_s}{nV_T}\right) - 1\right] - \frac{V + R_s I}{R_{sh}}$$

(18.36)

where:

I_o = diode reverse saturation current (A)

n = the diode ideality factor (between 1 and 2 for real diodes)

k = the boltzman constant (1.381 x 10^{-23} J/K)

q = the electron charge (1.602 x 10^{-19} Coulomb)

T_c = cell operating temperature (K)

As n is effectively an empirical factor that has to be estimated from the known data at the three measurement points, nV_T is sometimes regarded as a combined empirical factor, a (e.g. Duffie and Beckman, 1991). The extension of this formulation to a two-diode representation is straightforward but results in a further model parameter that has to be estimated (Masmoudi *et al*., 2016).

It is possible to make some simplifications of the one diode representation of a photovoltaic module. For example, for many modules the shunt resistance is very high and assuming infinite resistance results in small errors: this eliminates the right-hand term in Eqn. 18.36 Similarly, the 1 in the second term can be ignored with little error. This is the approach taken in the 2nd Edition of Duffie and Beckman (1991). This results in a model with four parameters that have to be estimated and models following this approach have been implemented in popular simulation tools (Klein et al., 1997; Crawley et al., 2001). If the shunt resistance is retained (e.g. as in Duffie and Beckman, 2013) then a fifth parameter has to be found.

The three empirically established reference *I-V* points – open circuit, short circuit and maximum power – can be substituted into Eqn. 18.36 to give relations for the model parameters: I_o, R_s, R_{sh}, n (or a) etc. However, other relationships need to be established to form a set of equations defining all four or five parameters. Details of different approaches as to how this may be done is explained elsewhere (e.g. Schroder, 1998). It is necessary to find these using numerical methods.

As the I-V characteristic is dependent also on cell operating temperature, it is further necessary to incorporate a method for calculating this in any model of a PV module or cell. A number of approaches are possible by defining a heat balance on the module and relating this to environmental variables. The heat balance can be formulated and a suitable heat transfer

parameter found by considering conditions at which the Nominal Operating Cell Temperature (NOCT) is measured (Table 18.4). Absorbed solar irradiation can be balanced against the portion converted into electrical power and heat lost from the module as follows,

$$\tau\alpha G_T = \eta_{mp} G_T + U_L(T_c - T_a) \tag{18.37}$$

where $\tau\alpha$ is the proportion of incident solar irradiation G_T (W/m^2) that is transmitted and absorbed (as in the discussion of thermal collectors above), is an overall heat transfer coefficient (W/m^{2}K) and T_a is the air temperature. The NOCT reference conditions are $T_a =$ 20ºC; $G_T = 800$W/m^2; wind speed 1m/s. As there is no current drawn from the module in test conditions ($\eta_{mp} = 0$) and substitute the test values the empirical parameters can be found from,

$$\tau\alpha/U_L = (T_{c,NOCT} - T_{a,NOCT})/G_{T,NOCT} \tag{18.38}$$

For the usual high transmittance low iron glass covering it is reasonable to take a value of 0.9 for $\tau\alpha$ (as Duffie and Beckmann (1991) suggest) so that we can use Eqn. 18.38 to find the overall module heat transfer coefficient (U_L). The cell temperature can then be calculated from the current air temperature and solar irradiation using,

$$T_C = T_a + \frac{G_T \tau\alpha}{U_L}\left(1 - \frac{\eta_{mp}}{\tau\alpha}\right) \tag{18.39}$$

Other formulations of heat balance involving more parameters (e.g. wind speed) have been suggested and are available in some software. Other forms of heat balance may furthermore be more appropriate for modules closely integrated with the fabric rather than those mounted on frames.

It should be noted that the equivalent diode representations of PV modules, as outlined above, result in an implicit equation (Eqn. 18.36) that has to be solved numerically along with that for cell temperature at each time step to find the operating point on the *I-V* curve. This requires some representation of the characteristics of the load, e.g. pump or battery, if the system for an 'off-grid' application. Otherwise, assuming the maximum power point is being tracked, the maximum power point has to be found by searching on the *I-V* curve to find the maximum power at each step.

In design calculations (e.g. using monthly climate data) it may be sufficient to use a model of intermediate complexity between one assuming fixed conversion efficiencies, and one with a detailed circuit representation. Such a modelling approach is described below following that of Duffie and Beckman (1991). This takes account of the effect of environmental temperature and irradiation on cell temperature – and therefore conversion efficiency – but does not calculate current and voltage explicitly. This could be thought of as a model capturing the first-order effects of variations in cell temperature on conversion efficiency. This modelling approach necessarily assumes that the module is always operating at its maximum power point and is therefore only suitable for building integrated systems using Maximum Power Point Tracking (MPPT) equipment. Although first presented as a design method using synoptic climate data, it can be used for hourly analysis where such data are available and is readily implemented in a spreadsheet.

The model is formulated firstly so that the variation in cell conversion efficiency is calculated according to cell temperature. The difference between the efficiency in test conditions and that at a particular cell operating temperature depends can be related to the published maximum power temperature coefficient ($\mu_{p,mp}$) and the corresponding temperature difference as follows,

$$\eta_{mp} = \eta_{mp,ref} + \mu_{p,mp}\left(T_c - T_{ref}\right) \tag{18.40}$$

where η_{mp} is the maximum power efficiency at the current time step, $\eta_{mp,ref}$ is the maximum power efficiency at Standard Test Conditions (STC) and T_{ref} is the STC reference temperature (25 °C). Although some manufacturers give a value for the coefficient ($\mu_{p,mp}$) it is most accurately calculated as, $\mu_{p,mp} = \eta_{mp,ref}\,\mu_{Vocp,mp}\,/V_{mp}$.

In order to arrive at a formulation that requires no iteration, the expression for cell temperature, Eq (18.39) can be substituted to give,

$$\eta_{mp} = \eta_{mp,ref} + \left[1 + \frac{\mu_{p,mp}}{\eta_{mp,ref}}\left(T_a - T_{ref}\right) + \frac{\mu_{p,mp}G_T}{\eta_{mp,ref}}\frac{\tau\alpha}{U_L}\left(1 - \frac{\eta_{mp}}{\tau\alpha}\right)\right] \tag{18.41}$$

The last term $\eta_{mp}/\tau\alpha$ can be approximated by $\eta_{mp,ref}$ with little error. This results in the final equation for module power conversion efficiency,

$$\eta_{mp} = \eta_{mp,ref} + \left[1 + \frac{\mu_{p,mp}}{\eta_{mp,ref}}\left(T_a - T_{ref}\right) + \frac{\mu_{p,mp}G_T}{\eta_{mp,ref}}\frac{\tau\alpha}{U_L}\left(1 - \eta_{mp}\right)\right] \tag{18.42}$$

This equation has parameters that can be entirely derived from manufacturers' data. Efficiency is expressed as a linear function of dry-bulb temperature and incident solar irradiation. As the coefficient $\mu_{p,mp}$ is always negative this formulation suggests a fall in efficiency on warm bright days as expected. In winter conditions cold atmospheric conditions will be shown to be advantageous for a given level of solar irradiation.

Example 18.4 solar photovoltaics

Using the data in Table 18.4 it is possible to calculate the overall heat transfer coefficient and the cell temperature when the ambient temperature is 3°C and the incident solar irradiation is 150W/m². The result of this calculation can be compared with that representing a summer condition: 28°C and 650 W/m².

Solution:

Firstly, it is necessary to calculate the overall heat transfer coefficient using Eq. 18.38 and the data from table 18.4 for the Normal Operating Cell Temperature (800 W/m² irradiation and 20°C). A value of 0.9 for $\tau\alpha$ is assumed as noted earlier. Hence

$$0.9/U_L = (47.0-20.0)/800 = 0.03375$$

so that $U_L = 26.67$ W/m².K.

The cell temperature can then be estimated from Eq. 18.39 using the nominal efficiency (13.9%) as follows,

$$T_c = 3.0 + 150 \times 0.03375\ (1 - 0.139/0.9) = 7.28\ ℃$$

Similarly, for the summer condition when the air temperature is 28 °C and the incident irradiation is 650W/m^2:

$$T_c = 28.0 + 650 \times 0.03375\ (1 - 0.139/0.9) = 46.55\ ℃$$

The significant difference in temperatures between winter and summer can be seen to be strongly driven by the solar irradiation. Note that these calculations assumed the nominal efficiency. A better solution could be obtained using Eq. 8.42 for the overall efficiency and then calculating the cell temperature, as suggested below in the chapter activity.

End of Solution.

In order to make some assessment of PV system output to the building AC power system, it is furthermore necessary to consider other factors detrimental to overall efficiency arising in the 'balance of system' and represented cumulatively by the term, η_e in Eqn. 18.32. A number of potential causes of loss can be identified. These may amount to very modest reductions in efficiency when considered alone, but cumulatively represent a noticeable effect that should be considered. A number of causes have been identified in the literature and have been noted in Table 18.5 These losses include those relating to the limitations in power point tracking, cable losses as well as those usually acknowledged relating to limited inverter efficiency. Some allowance for degradation from test conditions due to dust and dirt (soiling) may also be considered. Taken together these may give values for η_e in the range 0.85-0.95.

Although it is difficult to deal with some forms of inefficiency other than by estimated constant parameters, one important element in the overall efficiency of the balance of system is the behaviour of the inverter, which is known to be rather nonlinear. Over much of the working range of an inverter the efficiency of conversion of DC to AC power can be expected to be approaching a constant high value (greater than 95% in many instances). However, conversion efficiencies tend to drop-off to much lower values approaching the bottom of the working range. Example efficiency characteristics of inverter products are shown in Fig. 18.14.

In view of the importance of inverter performance and selection a good deal of test data is available and models are available that make use of such data to define empirical model parameters. The model developed at Sandia National Laboratory (King *et al.,* 2007) is well supported by manufacturers part-load performance data and is utilized in popular design software. The model represents behaviour in terms of a second-order polynomial to define the AC power output according to DC input at a given system voltage as follows,

$$p_{ac} = (p_{dc} - B)\left[(p_{aco}/(A - B)) - C(A - B)\right] + C(p_{dc} - b)^2 \qquad (18.43)$$

Table 18.5 – Possible PV system operational losses (After Firth, 2006).

Type of losses	Description	Report
Production variations and mismatch	PV module efficiency deviates from STC specification due to manufacturing process variations (+/- 5% over a sample of modules).	2, 3, 4,6
DC wiring losses	DC cable transmission losses – power transmitted at low voltage and high current results in noticeable losses.	3, 4,6
Inverter maximum power point tracking (MPPT)	MPPT may be imperfect where loads or irradiation vary rapidly.	1, 2, 3,6
Inverter DC-AC conversion	Loss in conversion of DC power to AC power	1, 3, 4,6
Inverter saturation	Occurs when the power input to the inverter exceeds the inverter rating (poor sizing).	5
Dirt and Dust	The panel glass cover transmittance is reduced over time by dirt and dust.	6

Sources: 1 - (Oozeki et al., 2003); 2 - (Stettler et al., 2005); 3 - (Reinders et al., 1999); 4 - (Kiefer et. al, 1995); 5 - (Ransom and Funtan, 2005); 6 – (CEC 2011)

Where:

$$A = p_{dco}\Big[1 + C_1(V_{dc} - V_{dco})\Big]$$

$$B = p_{so}\Big[1 + C_2(V_{dc} - V_{dco})\Big]$$

$$C = C_0\Big[1 + C_3(V_{dc} - V_{dco})\Big]$$

and,

p_{ac} = AC-power output from the inverter system

p_{dc} = DC-power input

V_{dc} = DC voltage input (a design value that may be different from the reference value)

P_{aco} = maximum AC power rating

P_{dco} = DC power at which the maximum AC power rating is achieved

V_{dco} = DC voltage at the reference condition

P_{so} = DC power required to start the inversion process

P_{so} = DC power required to start the inversion process

C_0 = empirical parameter defining the parabolic curvature about the reference power condition

C_1 = empirical parameter describing variation in p_{dco}

C_2 = empirical parameter describing variation in p_{so}

C_3 = empirical parameter describing variation in C_0 with DC voltage input.

This model, along with a sample of manufactures'' data, have been used to generate the characteristics shown in Fig 18.14. This shows some noticeable variation in performance at the bottom of the operating range. The nature of the characteristic also highlights the need for inverter capacity to be carefully matched with expected DC output. When this model is combined with the PV module model of conversion efficiency described by Eqn. 18.42, the combined effect of variations in environmental conditions and variations in inverter efficiency can be considered. The combined effects are well illustrated by plotting the ratio of the model output to that predicted by assuming a constant conversion efficiency.

Example system performance ratio data are shown in Fig. 18.15. These data are shown firstly as DC output from the modules (before inverter). Here the variations – that is the fall in efficiency with increased solar irradiation – are shown by the negative slope to the data and the scatter is due to variations in coincident dry-bulb temperature around a given level of solar irradiation. The further sets of data show the impact of variations in inverter efficiency and illustrate the variation between different manufacturers' models with the same nominal capacity.
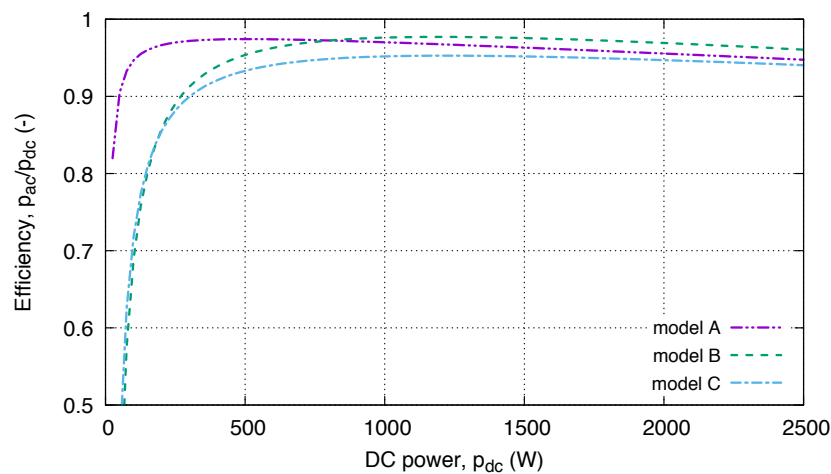

Figure 18.14. Example DC-AC inverter system efficiency characteristics (nominal capacity 2.5kW).
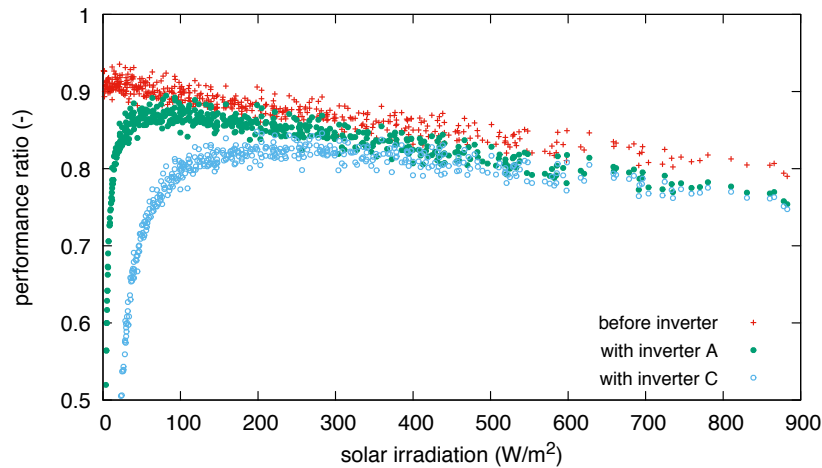
Figure 18.15. PV system performance ratio variation. Each point represents one hour in a summer month. Variations assuming different inverter models are shown along with modelled DC output (before inverter).

It can be seen that different levels of sophistication of the representation of photovoltaic panel systems are possible. Some models are amenable to spreadsheet calculation outside of building simulation tools and others may be available integrated into such tools or equation solving environments. Probably the level of sophistication chosen will depend on the modellers objectives at a given stage in a project and whether specific modules are inverters are selected and consequently if parameter data can be readily obtained.

Building wind power systems

Micro-scale wind turbines (say less than 50kW for current purposes) for off-grid applications are a relatively well understood technology and as reduction in carbon emissions has been of increasing concern, so to, attempts to integrate such wind turbines into building projects have grown. Consequently, in assessing demands and emissions from buildings it is desirable to make assessments of wind power generation potential in building simulation studies and so some of the key modelling issues are highlighted here. Details of particular turbine technologies are not dealt with as our focus is on overall power generation and relatively simple approaches to representing particular devices are all that is required.

In an ideal project, one would want to establish the variations in wind speeds at a particular site using anemometer devices and long-term data logging. This approach is rarely economic or practical and often some reliance must be made on other sources of wind data – at least at the early stages of project analysis. Using modelling methods to simulate operation of wind energy systems can be thought of as a five-step process:

1. selection of a wind data source;
2. calculation of wind speed at the wind turbine position;
3. calculation of power generation variations;
4. correction for other power conversion losses.
5. Integration and reporting of time-varying outputs.

It is important to recognize that there are uncertainties associated with each step in this process. In particular, the difficulties with estimating wind conditions in certain complex urban environments can mean that the uncertainty in any modelling result is high – possibly unacceptably so (Philips *et al.*, 2007). These uncertainties should be acknowledged in any analysis.

It is possible to state, in very general terms, that the power available from a wind turbine is a function of its swept area (*A*), air density (*ρ*) and effective wind speed (*U_e*) which can be expressed as,

$$p_{WT} = \eta_e f(A, \rho, U_e) \tag{18.44}$$

The term η_e is included to indicate the useful power output is reduced by other inefficiencies in the power conversion and distribution processes – in a similar way to the parameter defined for PV power production. The difference between modelling approaches depends on how this function is represented and, in particular, what is assumed about the effective wind speed. As the power available from the wind is a function of its kinetic energy the function is often expressed as a fraction of the theoretically available energy modified by a Power Coefficient C_P so that power output at a particular hub wind speed can be represented as,

$$p_{WT} = \eta_e \frac{1}{2} C_p A_s U_e^3 \tag{18.45}$$

There is a theoretical upper limit to the value of C_P for horizontal axis wind turbines (HAWT) known as the Betz limit: 0.59. In reality, and for micro-scale devices in particular, the value of C_P changes with wind speed. This theoretical relationship nevertheless highlights the sensitivity of any prediction of power output to wind speed. This sensitively is compounded by the steep variation in wind speed with height near the ground.

Recorded wind data are measured at a particular height at the weather station (often 10m) in open and flat locations (e.g. airports). Consequently, recorded wind speeds are most likely to be higher than those experienced locally in urban locations. It is accordingly necessary to consider the difference in local speed between the values recorded in standard weather records and that at the height of the wind turbine hub. In principle this can be done by applying mathematical functions that describe boundary layer velocity profiles.

In open landscapes the wind speed gradually increases from virtually zero at ground level and the boundary layer develops according to a recognisable logarithmic profile. In areas where there are trees hedges and buildings the air flow patterns near the ground become disrupted as the wake of the airflow around such objects generates turbulence and the regular wind speed profile does not develop at ground level but at some distance closer to the top of the obstructions. Such land features are said to increase effective 'surface roughness' and this can be expressed according to 'roughness length' (*z_0*) as illustrated in Table 18.6.

To find the wind speed at the height of the wind turbine hub it is necessary to be able to relate the local velocity U_z, at height z, to the velocity at the point of measurement U_{ref}. Both power-law and log-law relationships are used in wind engineering to describe this relationship. A common logarithmic profile definition is,

$$U_z = \frac{\ln\left(z/z_0\right)}{\ln\left(z_{ref}/z_0\right)} U_{ref}$$

<div align="right">(18.46)</div>

The effects of turbulence near the ground, and the corresponding modification of the wind boundary layer, is most significant in the urban environment where building, road and vegetation variations constitute a very 'rough' surface. This is particularly so in the centre of large cities where tower blocks or skyscrapers make for very large variations in surface level. This can be considered in the calculations by identifying a 'displacement' height (d) at which the effective wind velocity is taken to be zero. Panofsky and Dutton (1984) and Mertens (2003) suggest that this displacement can be taken to be 75% of the average building height ($\bar{h}_b$) so that,

$$d = 0.75\bar{h}_b$$

<div align="right">(18.47)</div>

After taking the displacement into account, the logarithmic relationship between height and reference velocity can be written as,

$$U_z = \frac{\ln\left((z-d)/z_0\right)}{\ln\left(z_{ref}/z_0\right)} U_{ref}$$

<div align="right">(18.48)</div>

The formula is not valid at heights below the displacement height. Mertens (2003) furthermore suggested prediction of wind speed using this approach (or similar analytical profiles) is not accurate below a height defined according to roughness length,

$$z \geq 20z_0 + d$$

<div align="right">(18.49)</div>

In urban terrain this suggests the wind profile cannot be reliably predicted using functions like this unless the height of interest (e.g. the turbine hub height) is some distance above the average roof line. Profiles calculated according to these guidelines are illustrated in Figure 18.16. In this figure the profile is shown dotted below the height given by Eqn. 18.49. This suggests some caution should be taken in calculating wind velocities at turbine hub height where the hub is relatively close to the roof line.

In order to estimate the available wind resources at a particular building location it is important to consider the relationship with adjacent objects and conditions immediately surrounding the building. In collections of buildings of similar height, a large part of the flow passes over the roofs, and lower parts of the buildings experience swirling flow and some degree of shelter. Where building heights are more variable, tall buildings can induce wakes that significantly effect adjacent buildings depending on wind direction. Consequently, in view of the uncertainty in calculating flows very near and directly above the roofs of buildings, applications of calculation methods such as those noted above should be applied cautiously.

Table 18.6. Variations in Surface Roughness Length (z₀) according to Terrain type.

Roughness Class	Roughness Length (m)	Terrain Type
0	0.0002	Water surface
0.5	0.0024	Completely open terrain with a smooth surface, e.g. concrete runways in airports, mowed grass, etc.
1	0.03	Open agricultural area without fences and hedgerows and very scattered buildings. Only softly rounded hills
1.5	0.055	Agricultural land with some houses and 8 metre tall sheltering hedgerows with a distance of approx. 1250 metres
2	0.1	Agricultural land with some houses and 8 metre tall sheltering hedgerows with a distance of approx. 500 metres
2.5	0.2	Agricultural land with many houses, shrubs and plants, or 8 metre tall sheltering hedgerows with a distance of approx. 250 metres
3	0.4	Villages, small towns, agricultural land with many or tall sheltering hedgerows, forests and very rough and uneven terrain
3.5	0.8	Larger cities with tall buildings
4	1.6	Very large cities with tall buildings and skycrapers

Example 18.5 wind power

Calculate the wind speed at a height of 16m in a small town environment with average building height 10m and where the local weather station recorded wind speed is 5m/s at 10m height?

Solution:

Firstly, the displacement height is estimated from Eq. 18.47 as: *d = 0.75 × 10 = 7.5m*

For a small town environment, the roughness length from Table 18.4 is 0.4 so that Eq. 18.47 gives,

$$U_z = \frac{\ln\left(\frac{(18-7.5)}{0.4}\right)}{\ln\left(\frac{10}{0.4}\right)} 5.0 = \frac{3.268}{3.219} 5.0 = 5.08 \text{ m/s}$$

Referring to Eq. 18.49, $z \geq 20z_O + d$, suggests the minimum height we should consider this reliable would be $20 \times 0.4 + 7.5 = 15.5$m. Note that this is somewhat above average roof level.

End solution.

Having noted that there is likely to be considerable uncertainty in predicting fluctuations in wind speeds in complex urban environments, it is nevertheless possible to adjust recorded wind speeds and arrive at time series data that can be used in power conversion calculations at a particular building site and design hub height. The question then, is how this can be related to power output?
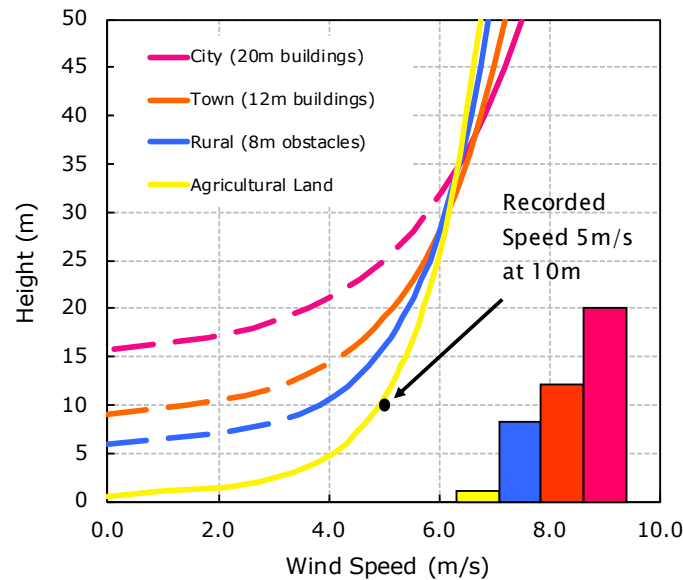

Figure 18.16. Logarithmic wind profiles calculated for different environments and corresponding roughness lengths. The profiles are calculated for a reference velocity of 5 m/s at a standard reference height of 10m. The rectangles indicate the respective mean building heights. Dotted lines indicate uncertainty in application of the profile as suggested by Eqn.49 and Mertens (2003).

Returning to Eqn. 18.45, it was noted that C_p tends to be variable in general. Fortunately, many micro-turbine manufactures provide data that allows power to be expressed as a function of hub wind speed – much as indicated in Eqn. 18.46. This data can be used in modelling the wind turbine device where the particular type of device is known. In this approach power output can be interpolated from the power curve data at each step using the wind data from a weather file that has been corrected for the turbine location and height. An example power curve is plotted in Fig. 18.17. This shows comparison with the theoretical limit (Eq. 45 with C_P=0.59) and illustrates that in practical turbines the wind speed has to rise above a cut-in value before it rotates. The profile is deliberately designed to flatten at higher wind speeds to ensure that the device is not damaged by severe wind conditions.

The power curve data will have been measured at standard atmospheric conditions (288.15K and 101325Pa). In hourly calculations it is possible to make corrections to the power data to account for the fact that the air density will be different at the site depending on climatic conditions. Coincident temperature and air pressure data are usually available from the same weather data source as recorded wind data. The power output at a particular step can be corrected according to the prevailing temperature and pressure as follows,

$$p_{WT,i} = \eta_e . p_{u,i}(U_{z,i})\left(\frac{P_i}{P_0}\right)\left(\frac{T_0}{T_i}\right)$$
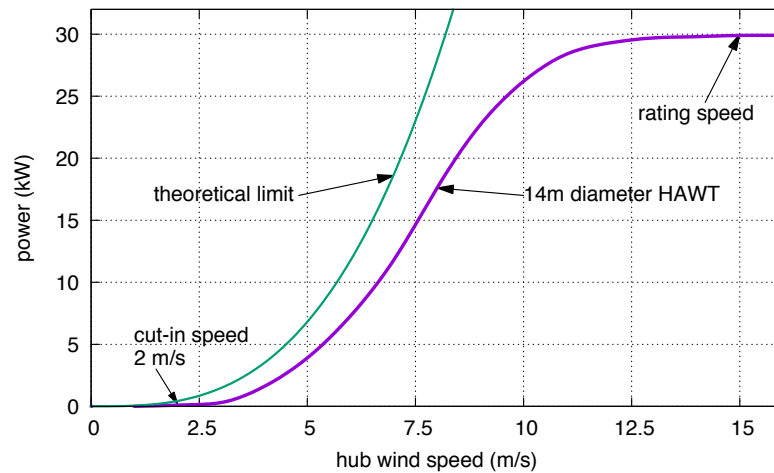
Figure 18.17 Example wind turbine power curve data for a horizontal axis wind turbine with nominal 30kW capacity at 15 m/s.

where, at time step i, $p_{WT,i}$ is the uncorrected power at local wind speed $U_{z,i}$, P_i and T_i are the atmospheric pressure and absolute temperature and P_0 and T_0 are the pressure and absolute temperature at standard measurement conditions (Gipe, 2004). This approach to calculation is not difficult to implement in spreadsheets or hourly building simulation tools. Data from an example calculation using the power curve in Fig. 18.17, is shown in Fig. 18.18. These data illustrate how wind power output falls to zero when the wind speed falls below the turbine cut-in speed of 2 m/s.
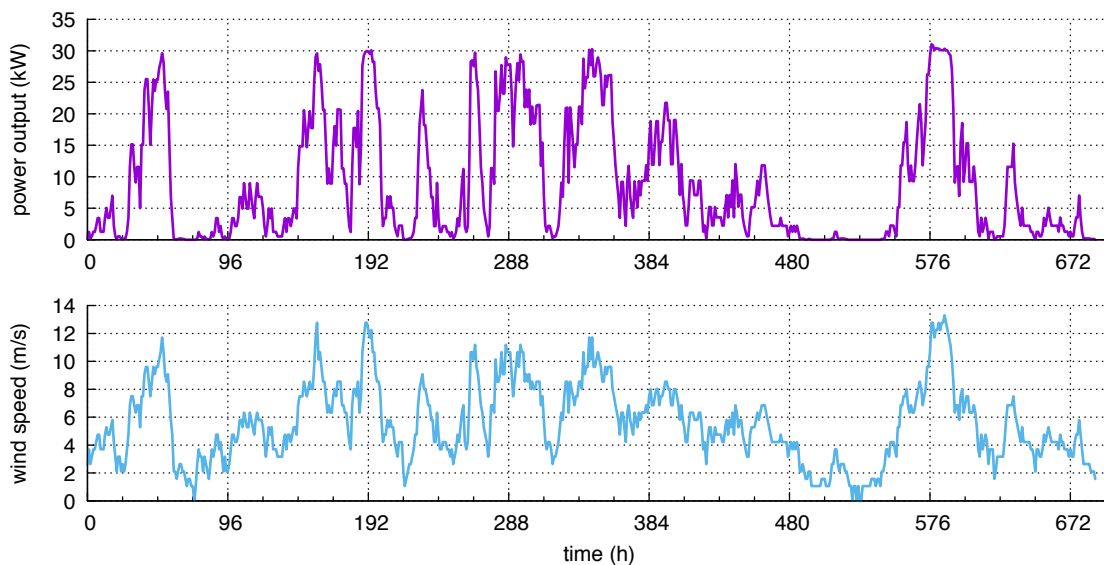

Figure 18.18. An example of wind power conversion calculated from manufacturers wind power curve data (Fig. 18.17) and hourly wind speeds (London, December data) calculated at hub height of 7m.

Geothermal heating and cooling

The interaction between the ground and the adjacent atmospheric environment along with the superior thermal capacity of the ground, are such that fluctuations in ground temperatures are always reduced in amplitude compared to the fluctuations in dry-bulb temperature. Making use of the grounds relatively high thermal capacity compared to either the air or typical building fabrics, is correspondingly thermodynamically advantageous when it comes to possible sources or sinks for heat pump systems. This is one main reasons for the abiding interest in geothermal heating and cooling using heat pumps (Ground Source Heat Pumps) as potentially one of the most efficient means of heating and/or cooling buildings.

Modelling and simulation of air source heat pumps can be said to be little more complex than other air-source refrigeration systems as it is straightforward to use the specified external air temperatures as boundary conditions when calculating heat transfer conditions on the source-side. Defining the fluid temperature conditions in ground-coupled heat pumps systems[1] is rather more complex and further models of ground heat transfer have to be employed in order to capture realistic variations in temperatures.

Transferring heat between a heat pump and the ground by embedding pipes in either shallow horizontal configurations (e.g. slinky loops), in much deeper vertical boreholes (e.g. using U-tubes) or in concrete elements of the building foundation system (e.g. concrete piles) allows coupling with a thermal capacity that is orders of magnitude greater than that of the building itself. This means that the behaviour of the system also has to be considered on much longer timescales than the building fabric. In fact, to model a ground coupled heat pump and its ground heat exchanger, both short time-scales have to be considered to capture heat transfer in the fluid and the region of ground close to the pipes (i.e. where ground temperature gradients are the greatest) and, very long timescales in order to consider the total heat exchange with the ground environment around the heat exchanger. It is fairly well understood that, over seasonal time scales, the ground heat exchanger will shift the temperatures in the surrounding region of the ground (on the scale of tens of metres) depending on whether the demands on the system amount to net heat rejection or heat extraction. For example, a building that rejects heat when considered over the whole season, may take as long as ten years before the average ground heat exchanger temperature reaches a steady-periodic pattern. This means that it is not feasible to design ground heat exchanger systems based on peak load conditions as might be done for other system components, and some form of long-term simulation is inevitable for both design (e.g. deciding on borehole depth and spacing) and performance prediction purposes (e.g. estimating system annual energy demands).

A number of models of borehole ground heat exchange systems have been developed. These can be broadly categorized as:

1. Analytical models;
2. Two-dimensional numerical models (e.g. Wetter and Huber, 1997);
3. Response factor models (e.g. Fisher *et al.* 2006);
4. Three dimensional numerical models (e.g. Diersch *et al.* 2011).

---

[1] Only closed-loop systems are considered here.

An example of the temperature field calculated after prolonged (50 year) application of a heat flux and calculated with a fully three-dimensional heat conduction solver is shown in Fig. 18.19 This illustrates a fully developed temperature field after net heat rejection in an array of 4 x 4 borehole heat exchangers. The variability of heat transfer between neighbouring boreholes can be seen in the horizontal cross-section such that the temperature in the central heat exchangers is greater than those at the perimeter. In the vertical cross-section it can be seen that at this timescale, the horizontal heat transfer is not two-dimensional but shows heat flow below the array and from the array towards the ground surface far from the centre of the array.
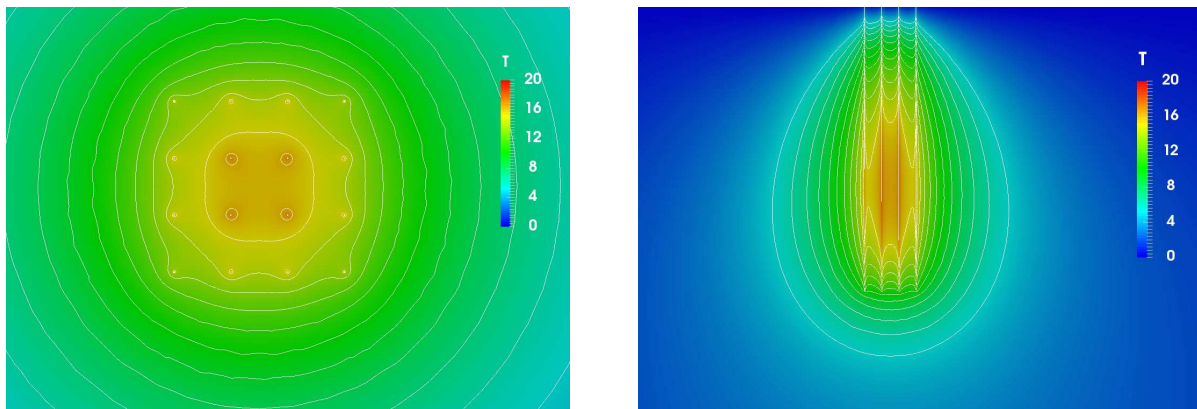
Figure 18.19. The long-term temperature field calculated for heat rejection in a 4 x 4 borehole heat exchanger array. A horizontal contour plane (left) and vertical plane (right). The contour lines show degree intervals.

The commonest approaches applied in design tools and system modelling (hourly or sub-hourly) are two-dimensional numerical models or forms of response factor methods. A number of variations of two-dimensional numerical models represent the flow of fluid in a single U-tube as a series of vertical nodes that are connected horizontally with resistances representing conduction between the pipes, the borehole wall and the surrounding ground. Heat capacity can be represented at some or all of the nodes and often heat transfer in the vertical direction in the surrounding ground is ignore i.e. the model is quasi two-dimensional. Such models are applicable to single boreholes as they often do not represent interaction between neighbouring boreholes.

In a number of design tools and widely used simulation tools, response factor approaches are used. These approaches have the advantage of being relatively fast to execute and capable of representing the important three-dimensional effects is arrays of borehole heat exchangers. In some of these approaches, and in design calculations, it is common to divide the timescales under consideration and to regard heat transfer within the borehole as steady-state such that it can be defined by a thermal resistance which when averaged over the depth of the borehole can be defined as, R_b (K.W/m):

$$R_b = \frac{(\bar{T}_f - T_b)}{q_b} \tag{18.51}$$

where $\bar{T}_f$ is the mean borehole fluid temperature, T_b is the borehole wall temperature and q_b (W/m) is the heat flux per unit depth at the borehole wall. This resistance is dependent on a number of factors in a typical U-tube borehole heat exchanger. Besides the pipe and grout thermal conductivities it is also dependent on the spacing between the pipes and their relative position in the borehole as well as borehole size and pipe dimensions. It should also be noted that this resistance includes the convective resistance between the fluid and the pipe walls and so is dependent on the flow conditions and fluid properties – these being noticeably variable with the low flow rates and high glycol content found in many installations. A typical borehole with a single U-tube is illustrated in Fig. 18.20 along with the resistance network representation.
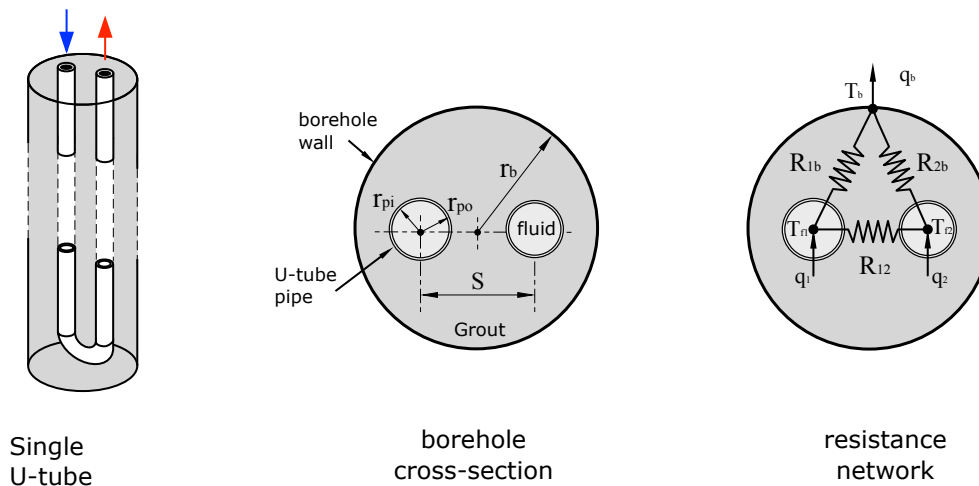

Figure 18.20. A typical single U-tube borehole heat exchanger and the representation of thermal resistances inside the borehole.

Javed and Spitler (2016) have given a systematic overview of the methods that can be used to calculate borehole resistance. These range from simplified correlations to highly accurate analytical methods.

Heat transfer around borehole heat exchanger arrays is commonly taken to be by conduction only (homogeneous material and no groundwater flow) and is represented mathematically by a linear diffusion equation: Fourier's equation. This allows the solution of time series to be found using super-position principles (Duhamel's theorem). This can be applied both spatially and temporally. It can further be taken that responses to input steps can be normalized by thermal conductivity and timescales by thermal diffusivity. For example, a normalized timescale, t_s, can be defined as:

$$t_s = \frac{H^2}{9\alpha} \tag{18.52}$$

where H is the depth of the borehole (m) and α is the thermal diffusivity of the ground (m²/s). It is firstly useful to apply super-position in the spatial sense. This allows the response

(temperature at the end of an applied heat step) of a complete borehole array to be calculated by super-imposing the response to a single borehole. The calculation of the response of a single borehole to a step in heat flux can be found by making a numerical calculation in cylindrical coordinates (i.e. 2D about the borehole axis) and the effective 3D effect found by super-position (Hellström, 1991). Corresponding analytical approaches have also been developed (Spitler and Javed, 2016). The responses consequently reflect the proper long-term interaction between borehole heat exchangers. Such response factors are termed 'g-functions' and examples are shown with respect to the log of t/t_s in Fig. 18.21 One noticeable feature of these data, are that at short timescales (a number of weeks in practice) the responses all converge to the response of a single heat exchanger. This is to be expected as at short timescales heat has not penetrated to the point of having a noticeable effect on neighbouring boreholes.

Applying the 'g-function' response factor consequently allows the borehole temperature, T_b, to be found relative to the undisturbed (initial) ground temperature, T_g, from application of a single heat step as follows:

$$T_b = T_g + \frac{q}{2\pi k^*} \cdot g(t/t_s) \tag{18.53}$$

where q is the heat flux of the pulse per unit length and k^* is the effective thermal conductivity of the ground and the function g is for a particular borehole array geometry. In a calculation with time-varying boundary conditions, as in a system simulation or design calculation, the time-varying temperature can be found by super-imposing the response to individual steps in heat flux as follows:

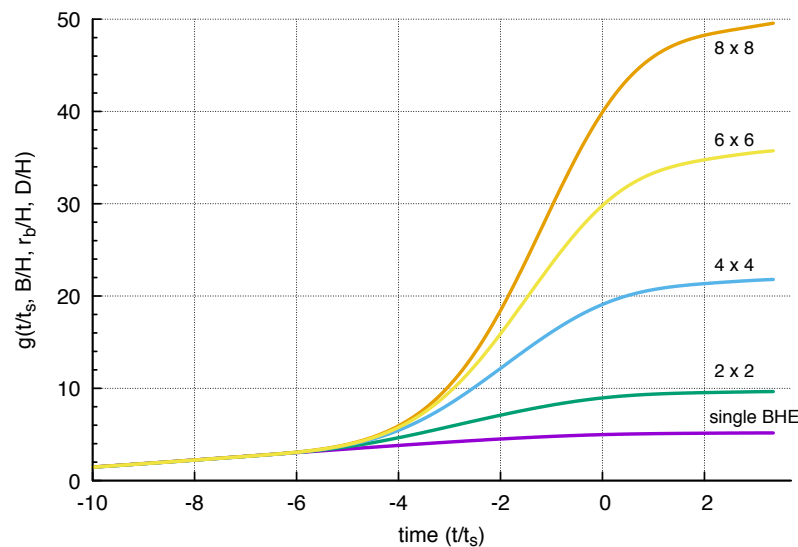$$T_b = T_g + \sum_{i=1}^{n} \frac{(q_i - q_{i-1})}{2\pi k^*} \cdot g(t/t_s) \tag{18.54}$$

Figure 18.21. Examples of borehole heat exchanger array 'g-function' data.

In general, g-functions are not simply functions of time but also borehole geometric configuration. They can then be normalized for given ratio of borehole spacing to depth, *B/H*, and the ratio of borehole radius to depth, r_b/H. Furthermore, in general the top of the heat exchanger does not rise to the surface but is some depth D below the surface. Hence, the functions should also be differentiated by the ratio *D/H*. Accordingly, in design and simulation tools it is convenient to refer to a library of such functions depending on key design parameters and possibly interpolate between some of the data.

At short time-scales (of the order of hours) most of the changes in thermal conditions occur within or close to the borehole. In a system simulation that works with small time steps (hourly or sub-hourly) a constant borehole resistance is not a good assumption. This is not an issue in design tool calculations where only long timescales are applicable. For system simulations the response functions must be adapted to account for short timescale effects. Yavuzturk and Spitler (1999) showed how g-functions can be extended to short times by calculating responses numerically with a model that included the details of the components inside the borehole i.e. the pipes and grout material. This is less generalizable (i.e. the calculated response is specific to a particular size/arrangement of pipes) but can be blended with the respective long timescale g-function data to allow both short and long timescales to be dealt with.

An example of a long-term calculation made with such a model (Fisher *et al.,* 2006) is shown in Fig. 18.22. Results using three different sizes of borehole array are shown for a building with predominant cooling loads. The average fluid temperature can be seen to follow the annual building loads and also shows year-on-year increases until a steady-periodic pattern is approached after approximately ten years. This highlights the need to carry out multi-year simulations if the sustainability of the system is to be predicted realistically.
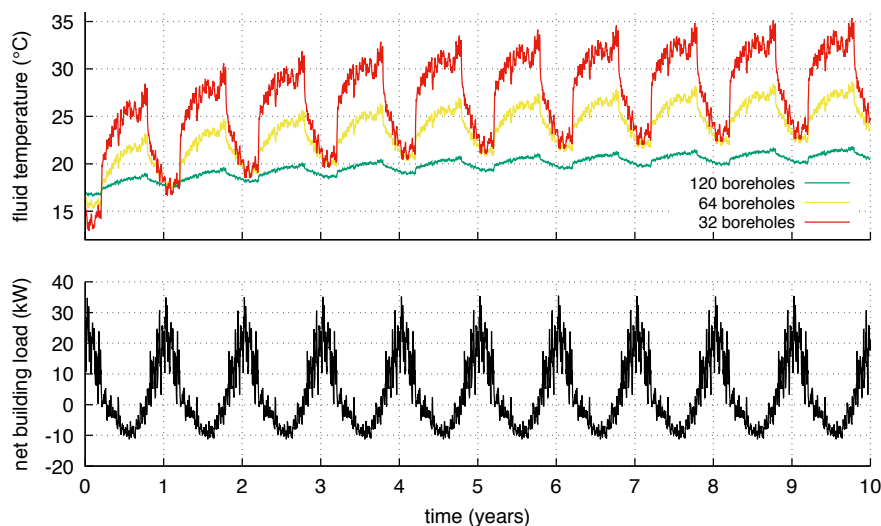

Figure 18.22. Borehole heat exchanger system fluid temperatures predicted over a ten-year period with different array sizes. The corresponding building loads are shown in the lower part of the figure (after Fisher et al., 2006).

Simulation of borehole heat exchanger response is necessary in a simplified way in selecting or sizing ground heat exchangers. A common approach would be to calculate long-term

response using large time steps e.g. derived from monthly energy exchange and peak heat transfer rates imposed over a few hours. If the objective is to design so as to maintain the minimum or maximum temperatures within certain limits (perhaps defined by heat pump limiting temperatures or a target heat pump efficiency) the response can be simulated and the borehole length adjusted until a design size is arrived at (Spitler and Bernier, 2016).

In whole system simulations, models are formulated to deterministically predict heat transfer rates and outlet temperatures given specified inlet flow rates and temperature. As simulation progresses, responses are calculated by keeping track of heat exchange at previous time steps and 'looking up' the response of each according to the appropriate g-function. After some long period, assumptions can be made about the sensitivity to past responses and historic fluxes aggregated together (Yavuzturk and Spitler, 1999). The types of parameters that are typically required in such models is shown in Table 18.7 along with possible data sources.

Table 18.7 Parameters typically defined for borehole heat exchanger models and possible data sources.

Model parameter	Possible data source
Borehole length, H	Design tool output or specialist contractor proposal
Borehole radius, R_b	Design tool output or specialist contractor proposal
Borehole spacing, B	Design tool output or specialist contractor proposal
Borehole sub-surface depth, D	Design assumption or specialist contractor proposal
Array configuration, (A x B) or total number of boreholes	Design tool data
Borehole thermal resistance	Design tool output
Ground thermal conductivity	Thermal response test or geological survey
Grout/backfill thermal conductivity	Grout manufacturers data
Ground and grout specific heat capacity	Grout manufacturers data
Ground and grout density	Response test data or geological survey
U-tube pipe size	Hydraulic system design data
U-tube pipe spacing	Design tool output or contractor proposal
Pipe thermal properties	Pipe manufacturers or Design Guide data
Fluid properties	Antifreeze manufacturers or Design Guide data

As models such as those using the g-function approach rely on the relationships between mean borehole fluid temperature and heat exchange, some assumptions are necessary about the relationship between this temperature and both the inlet and outlet temperature (Rees,

2015). A further question in modelling ground heat exchange systems is the impact of the transport of fluid along the long pipe lengths usually involved – both in terms of the large heat capacity of the fluid and also the fact that it may take fluid a few minutes or more to traverse the loop. In the type of quasi-3D nodal models described above, fluid transport up and down the borehole is accounted for explicitly and the physical effects are captured to some degree. Otherwise some representation of the effects can be made by coupling the heat exchanger model with discretized pipe models (Rees, 2015).

References

ARI (1998) *ARI Standard 550/590-98 – Water Chilling Packages using the Vapour Compression Cycle*. Arlington, VA: Air Conditioning and Refrigeration Institute.

ASHRAE (2016). Handbook of Systems and Equipment, Solar Energy and Equipment, p37.9.

Bertagnolio, B. & Lebrun, J. (2008) Simulation of a building and its HVAC system with an equation solver: Application to benchmarking. Building Simulation 1 pp.234-250.

BSI (2008a) BS EN 442-3: *Specification for Radiators and Convectors*. (London: The British Standards Institution.)

BSI (2008b) BS EN 14825: 2008. Air Conditioners, Liquid Chilling Packages and Heat Pumps with Electrically-driven Compressors for Space Heating and Cooling: Testing and Rating at Part Load Conditions. (London: The British Standards Institution.)

BSI (2015). BS EN 13203-2:2015. Gas-fired domestic appliances producing hot water. Part 2: Assessment of energy consumption. (London: The British Standards Institution.)

CEC. (2011). Emerging Renewables Program Guidebook (Twelfth Edition). California Energy Commission. 52 p.

Chow, T.T., Clarke, J.A. & Dunn, A. (1997) Primitive parts: An approach to air-conditioning component modelling. Energy and Buildings 26 pp.165-173.

Crawley DB, Lawrie LK, Pedersen CO, Strand RK, Liesen RJ, Winkelmann FC, (2001) EnergyPlus: Creating a New-Generation Building Energy Simulation Program. Energy and Buildings. 33(4):319–31.

Duffie JA, Beckman WA. (1991). Solar Engineering of Thermal Processes. 2nd Ed. Solar Engineering of Thermal Processes. New York: Wiley. 919 p.

Duffie JA, Beckman WA.(2013). Solar Engineering of Thermal Processes. 4th Ed. Hoboken, New Jersey: Wiley. 910 p.

F_Chart Software (2011) EES – Engineering Equation Solver. Available at: http://www.fchart.com/ees/ (Accessed: 15th December 2017).

Firth SK. (2006). Raising Efficiency in Photovoltaic Systems: High Resolution Monitoring and Performance Analysis. PhD Thesis: De Montfort University.

Fisher, D. E., Rees, S. J., Padhmanabhan, S. K., Murugappan, A., (2006). Implementation and Validation of Ground-Source Heat Pump System Models in an Integrated Building and System Simulation Environment. International Journal of HVAC&R Research 12(3a), 693-710.

Diersch, H.-J. G., Bauer, D., Heidemann, W., Ruhaak, W., Schatzl, P., 2011. Finite element modeling of borehole heat exchanger systems Part 1. Fundamentals. Computers & Geosciences 37, 1122-1135.

Fong, J., Edge, J.S., Underwood, C.P., Tindale, A. & Potter, S.E. (2015) Performance of a dynamic distributed element heat emitter model embedded into a third-order lumped parameter building model. Applied Thermal Engineering 80 pp. 279-287.

Gipe P. (2004). Wind Power: renewable energy for home, farm and business. Second Edition. White River Junction, Vermont: Chelsea Green Publishing. 512 p.

Gomaa, A.G., Underwood, C.P., Bond, T.J. & Penlington, R. (2002) Experimental investigation of sensible heat transfer in fin-and-tube cooling coils. Building Services Engineering Research and Technology 23(3) pp.197-204.

Hellström G. (1991) Ground Heat Storage: Thermal Analysis of Duct Storage Systems. PhD Thesis: University of Lund.

Hydronics Institute (1990) *Testing and Rating Standard for Baseboard Radiation.* Berkeley Heights, NJ: Hydronics Institute.

Javed S, Spitler JD. (2016). Calculation of borehole thermal resistance. In: Rees SJ, editor. Advances in Ground-Source Heat Pump Systems (Chapter 3) Woodhead Publishing. p. 63–95.

Kays, W.M. and London, A.L. (1964) Compact Heat Exchangers. 2nd ed. New York: McGraw-Hill.

Kiefer K, Körkel T, Reinders A, Rössler E, Wiemken E. (1995). PV roofs in Germany--operating results from intensified monitoring and analysis through numerical modeling. In: 13th European Photovoltaic Solar Energy Conference, Nice1995. p. 575–9.

King DL, Gonzalez S, Galbraith GM, Boyson WE. (2007). Performance Model for Grid-Connected Photovoltaic Inverters. Sandia technical report SAND2007-5036. Albuquerque.

Klein, S.A. (1975) Calculation of flat plate collector loss coefficient. Solar Energy 17 pp. 79-80.

Klein SA, Beckman WA, Mitchell JW. TRNSY - A transient system simulation program. Madison, WI, USA; 1997.

Masmoudi F, Ben Salem F, Derbel N. (2016). Single and double diode models for conventional mono-crystalline solar cell with extraction of internal parameters. In: 13th International Multi-Conference on Systems, Signals and Devices, SSD 2016. p. 720–8.

Mertens, S. (2003). The Energy Yield of Roof Mounted Wind Turbines, Wind Engineering 27(6): 507-516.

Modelica (2010) A Unified Object-oriented Language for Physical Systems Modeling. Available at: https://www.modelica.org/documents/ModelicaSpec32.pdf (Accessed: 15th December 2017).

Oozeki T, Izawa T, Otani K, Kurokawa K. (2003). An evaluation method of PV systems. Solar Energy Materials and Solar Cells. 75(3–4):687–95.

Panofsky, H.A., Dutton, J.A., (1984). Atmospheric turbulence, Models and Methods for Engineering, John Wiley & Sons.

Phillips, R., P Blackmore, J Anderson, M Clift, A Aguilo-Rullan and S Pester. (2007) *Micro-wind turbines in urban environments: an assessment'* BRE Trust report FB17, ISBN 978-1-84806-021-0.

Ransome S, Funtan P. (2005). Why hourly averaged measurement data is insufficient to model PV system performance accurately. In: 20th European Photovoltaic Solar Energy Conference, Barcelona.

Rees SJ. (2015). An extended two-dimensional borehole heat exchanger model for simulation of short and medium timescale thermal response. Renewable Energy. 83:518–26.

Reinders A, Van Dijk VAP, Wiemken E, Turkenburg WC. (1997). Technical and economic analysis of grid-connected PV systems by means of simulation. Prog Photovoltaics Res Appl. Wiley Online Library;7(1):71–82.

Sahlin, P., Eriksson, L., Grozman, P., Johnsson, H., Shapovalov, A. & Vuolle, M. (2004) Whole-building simulation with symbolic DAE equations and general purpose solvers. Building and Environment 39 pp. 949-958.

Schroder DK. (1998). Semiconductor Material and Device Characterization, 3rd Edition. In: Semiconductor Material and Device Characterization (Internet). Third. New York: Wiley. p. 522

SPARK (2010) Simulation Problem Analysis and Research Kernel (spark). Available at: http://eta.lbl.gov/resources/software/spark (Accessed: 15th December 2017).

Spitler JD, Bernier M. (2016). Vertical borehole ground heat exchanger design methods. In: Rees SJ, editor. Advances in Ground-Source Heat Pump Systems. Oxford: Woodhead Publishing. p. 29–61.

Stettler S, Toggweiler P, Wiemken E, Heydenreich W, de Keizer AC, van Sark W, (2005). Failure detection routine for grid-connected PV systems as part of the PVSAT-2 project. In: Proceedings of the 20th European Photovoltaic Solar Energy Conference & Exhibition, Barcelona, Spain. p. 2490–3.

Trčka, M. & Hensen, J.L.M. (2010) Overview of HVAC system simulation. Automation in Construction 19 pp.93-99.

Underwood, C.P. (1998) *HVAC Control: Modelling, Analysis and Design.* London: Taylor & Francis.

Underwood, C.P. & Yik, F.W.H. (2004) Modelling Methods for Energy in Buildings. Chapter 5. Oxford: Wiley-Blackwell.

Underwood, C.P., Shepherd, T., Bull, S.J. & Joyce, S. (2018) Hybrid thermal storage using coil-encapsulated phase change materials. Energy and Buildings 159 pp. 357-369.

Wetter, M., Huber, A., 1997. TRNSYS Type 451: Vertical Borehole Heat Exchanger EWS Model, Version 3.1 - Model Description and Implementing into TRNSYS. Transsolar GmbH, Stuttgart, Germany.

Yavuzturk, C., Spitler, J. D., (1999). A Short Time Step Response Factor Model for Vertical Ground Loop Heat Exchangers. ASHRAE Transactions 105(2), 475-485.

Yik, F.W.H., Lai, J.H.K., Fong, N.K., Leung, P.H.M. & Yuen, P.L. (2012) A case study on the application of air- and water-cooled oil-free chillers to hospitals in Hong Kong. Building Serv. Eng. Res. Technol. 33(3) pp. 263-279.

Recommended Reading

Readers seeking further details of the material presented hear on HVAC modelling and control are referred to the book by Underwood and Yik (2004). The book 'Solar Engineering of Thermal Processes' (2013) has been through a number of editions and remains a very useful source of reference material regarding solar thermal and photovoltaic technologies. For readers seeking further details of both wind power technology and models, the book by Paul Yipe serves as a good introduction. A multi-author reference on geothermal systems was published in 2016 'Advances in Ground Source Heat Pump Systems' and provides much further detail on borehole heat exchanger modelling, calculation of borehole resistance and a range of geothermal technologies.

Activities

This suggested activity can be used to gain some insight into how PV output can be calculated from basic simulation data and how it can be expected to vary. This can be carried out in a spreadsheet tool. Firstly, choose a solar panel product and extract the relevant performance coefficients such as those given in Table 18.4. Either from a simulation weather file or simulation tool output, select a time series of solar irradiation and coincident dry-bulb temperatures and insert them into two columns of the spreadsheet. From the performance data, calculate the heat transfer coefficient data as shown in the example. You can then use Eq. 18.42 to calculate the efficiency at each step. It is convenient to express Eq.18.42 as follows when using a spreadsheet:

$$\eta_{mp} = \eta_{mp,ref} \left[A + B \times T_a + C \times I_T \right] \tag{18.55}$$

The constants *A, B* and *C* are then,

$$A = 1 - \frac{\mu_{P,mp}}{\eta_{mp,ref}} T_{ref}, \qquad B = \frac{\mu_{P,mp}}{\eta_{mp,ref}}, \qquad C = \frac{\mu_{P,mp}}{\eta_{mp,ref}} \frac{\tau\alpha}{U_L} \left(1 - \eta_{mp,ref}\right) \tag{18.56}$$

These constants are calculated from the manufacturers data (Table 18.4) and need be computed only once (e.g. at the start of the spreadsheet). You can then generate a time-series for the efficiency. This can be supplemented by a calculation of cell temperature using Eq. 18.39 and overall output using Eq.18.32. For additional interest, readers can add an inverter model to

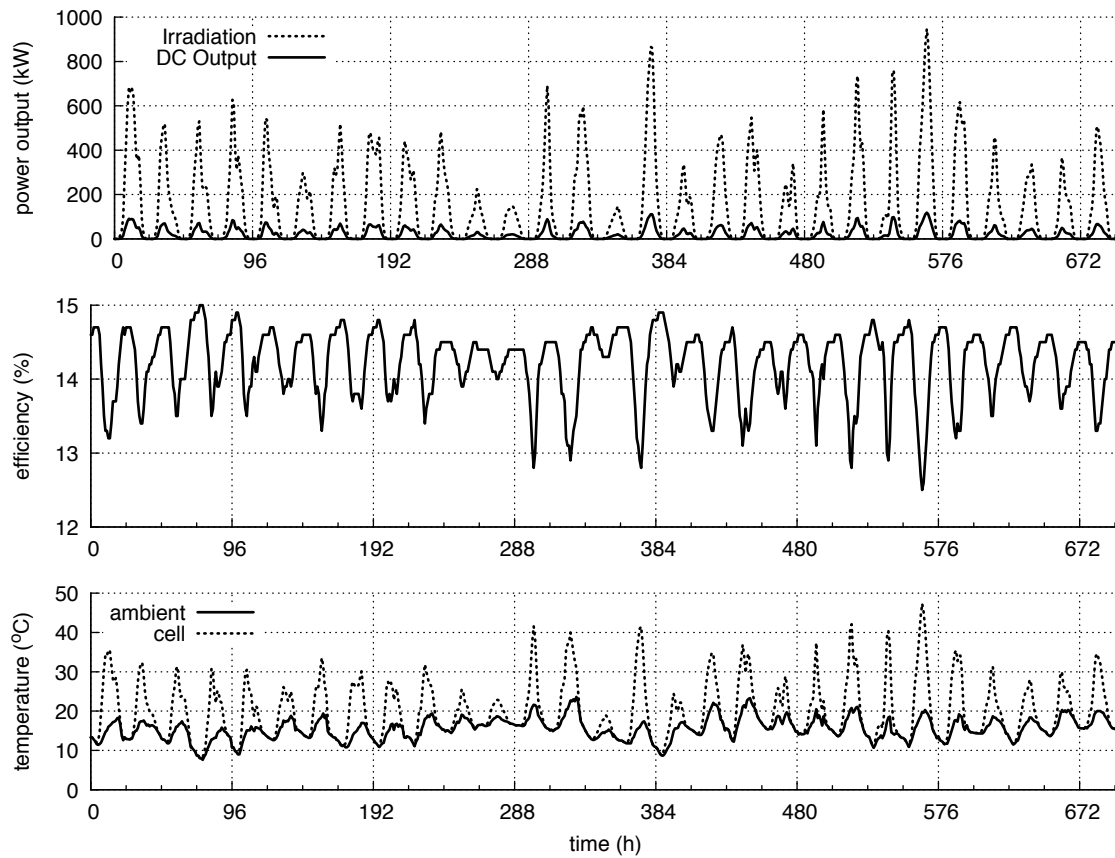calculate AC output. Example output that could be expected from this activity is shown in Figure 18.23.

Figure 18.23. Example output from the chapter activity.